A Spectral Method to Compute the Tides of Laterally Heterogeneous Bodies

Rovira-Navarro, Marc; Matsuyama, Isamu; Berne, Alexander

Important note
To cite this publication, please use the final published version (if applicable).
Please check the document version above.

A Spectral Method to Compute the Tides of Laterally Heterogeneous Bodies

Marc Rovira-Navarro[1,2] , Isamu Matsuyama[1] , and Alexander Berne[3]

[1] Lunar and Planetary Laboratory, University of Arizona, Tucson, AZ 85721, USA
[2] Faculty of Aerospace Engineering, TU Delft, Building 62 Kluyverweg 1, 2629 HS Delft, The Netherlands
[3] California Institute of Technology, Pasadena, CA 91125, USA

Abstract

Body tides reveal information about planetary interiors and affect their evolution. Most models to compute body tides rely on the assumption of a spherically symmetric interior. However, several processes can lead to lateral variations of interior properties. We present a new spectral method to compute the tidal response of laterally heterogeneous bodies. Compared to previous spectral methods, our approach is not limited to small-amplitude lateral variations; compared to finite element codes, this approach is more computationally efficient. While the tidal response of a spherically symmetric body has the same wavelength as the tidal force; lateral heterogeneities produce an additional tidal response with a spectra that depends on the spatial pattern of such variations. For Mercury, the Moon, and Io, the amplitude of this signal is as high as 1%–10% of the main tidal response for long-wavelength shear modulus variations higher than $\sim 10\%$ of the mean shear modulus. For Europa, Ganymede, and Enceladus, shell-thickness variations of 50% of the mean shell thickness can cause an additional signal of $\sim 1\%$ and $\sim 10\%$ for the Jovian moons and Enceladus, respectively. Future missions, such as BepiColombo and JUICE, might measure these signals. Lateral variations of viscosity affect the distribution of tidal heating. This can drive the thermal evolution of tidally active bodies and affect the distribution of active regions.

Unified Astronomy Thesaurus concepts: Solid body tides (2298); Planetary interior (1248); Natural satellites (Solar system) (1089)

1. Introduction

The deformation of planets and moons under a tidal force depends on their internal properties—e.g., density stratification, as well as elastic and anelastic properties. As a consequence, observations of body tides can be used to infer the internal properties of planetary objects (e.g., Segatz et al. 1988; Konopliv & Yoder 1996; Hoppa et al. 1999; Wahr et al. 2006; Hamilton et al. 2013; Sohl et al. 2014; Williams & Boggs 2015; Steinbrüugge et al. 2018).

Traditionally, body tides have been studied under the assumption of spherical symmetry, i.e., the internal properties of the body only vary radially and not laterally. However, planets and moons are not spherically symmetric. Seismic tomography evidences that Earth's lithosphere and mantle are not spherically symmetric but present lateral structures associated with tectonics and deep mantle dynamics (Woodhouse & Dziewonski 1984; Ritsema et al. 2011); the Moon shows a farside–nearside dichotomy in crustal thickness (Neumann et al. 1996; Wieczorek et al. 2013); and Mars has a well-known northern–southern hemisphere dichotomy (Neumann et al. 2004; Watters et al. 2007), as does the ocean world Enceladus (Porco et al. 2006; Crow-Willard & Pappalardo 2015; Čadek et al. 2016; Beuthe et al. 2016; Park et al. 2024).

Lateral variations of internal properties affect the tidal response of a body. If a body is spherically symmetric, the tidal response is proportional to the tidal forcing—the body responds with a mode of the same wavelength as that of the forcing. In contrast, when internal properties vary laterally, modes of different wavelength are coupled and the tidal response contains modes of wavelengths other than that of the forcing (e.g., Berne et al. 2023b). The tidal response spectrum contains information about the amplitude and patterns of lateral variations; hence, it can be used to constrain such variations—a technique known as tidal tomography (e.g., Métivier et al. 2007; Zhong et al. 2012; Qin et al. 2014, 2016; Lau et al. 2017). Lateral variations of anelastic properties affect the distribution of tidal energy dissipation within the interior (Steinke et al. 2021), affecting the evolution of the interior and resulting in distinct surface features.

The tidal response of a spherically symmetric body is often obtained by solving the equations governing the deformation of a self-gravitating body using a spectral method with spherical harmonics as basis functions. The properties of spherical harmonics allow to transform the 3D governing differential equations into a set of equations with radial dependence only. Love (1911) first used this approach to obtain the tidal response of a self-gravitating homogeneous elastic body. Since then, the approach of Love has been extended to radially stratified bodies (e.g., Alterman et al. 1959; Takeuchi et al. 1962; Jara-Orué & Vermeersen 2011) and to include anelastic effects (e.g., Peltier 1974; Ross & Schubert 1986; Wahr & Bergen 1986; Segatz et al. 1988). This approach is computationally inexpensive and allows to tackle the inverse problem—given the tidal response of a body, inferring its interior properties.

Mode coupling makes it more complicated to obtain the tidal response of a body with lateral heterogeneities. Several methods have been developed to tackle the problem. Finite element methods (FEM) have been employed for tidal (e.g., Métivier et al. 2006; Latychev et al. 2009; Zhong et al. 2012; A et al. 2014; Souček et al. 2016, 2019; Steinke et al. 2021; Zhong et al. 2022; Berne et al. 2023a) and surface loads (e.g., Wu 2004; van der Wal et al. 2013). Alternatively, spectral methods can be used. Martinec and collaborators have

developed a numerical spectral-finite element approach to obtain the response of a self-gravitating viscoelastic Earth to surface loads (Martinec 2000; Tanaka et al. 2011, 2021). In their approach, the angular dependence of the solution is expanded using tensor spherical harmonics and the resulting equations solved using finite elements in the radial direction. Numerical methods are very flexible, but they are computationally expensive, making them unsuitable to solve the inverse problem. To overcome this limitation, several authors have developed inexpensive semi-analytical spectral methods. However, existing methods either rely on perturbation theory, and thus are only applicable to bodies with small lateral heterogeneities (Qin et al. 2014; Lau et al. 2015; Qin et al. 2016; Lau et al. 2017), or on thin-shell theory, and are therefore limited to bodies that have a thin outer shell overlying a fluid layer (Beuthe 2018, 2019).

The aim of this work is to present a new spectral method that combines the flexibility of numerical methods with the computational efficiency of semi-analytical spectral methods and apply it to consider the tidal response of bodies with lateral heterogeneities. As opposed to spectral-perturbation methods, our method does not require lateral variations to have a small amplitude. Compared to the spectral-finite-element method of Martinec (2000) and Tanaka et al. (2021), angular integrals are performed analytically using the properties of tensor spherical harmonics, rather than numerically, and the equations are solved in the Fourier domain, rather than in the time domain (as done for lateral variations of viscosity in Martinec 2000) or iteratively (as done for lateral variations of elastic properties in Tanaka et al. 2021).

The paper is structured as follows. Section 2 introduces the viscoelastic-gravitational problem, and in Sections 3 and 4, the governing equations are transformed to the spectral domain and solved. In Section 5, we compare the new spectral method with a spectral-perturbation method and an FEM code, and in Sections 6 and 7, we obtain the tidal responses of elastic and viscoelastic bodies with various types of lateral heterogeneities to illustrate their effect on the tidal response. The paper finishes with a summary of the main results in Section 8.

Alongside with this paper, we release the *LOV3D* software package, which uses the method described here to compute the tidal response of laterally heterogeneous bodies (Rovira-Navarro 2024).

2. Problem Formulation

2.1. Governing Equations

The tidal response of a self-gravitating body can be obtained by solving the mass, momentum, and Poisson's equation. The equations are linearized around a state of hydrostatic equilibrium with gravitational potential ϕ_0 and pressure p_0 given by $\nabla p_0 = -\rho_0 \nabla \phi_0$ and $\nabla^2 \phi_0 = 4\pi G \rho_0$, where G is the universal gravitational constant and ρ_0 the density of the unperturbed body. The resulting equations are then (e.g., Sabadini et al. 2016):

$$\rho' = -\rho_0 \chi - \boldsymbol{u} \cdot \nabla \rho_0, \tag{1a}$$

$$\nabla \cdot \boldsymbol{\sigma}' - \rho_0 \nabla(g\boldsymbol{u} \cdot \boldsymbol{e_r}) + g\rho_0 \chi \boldsymbol{e_r} - \rho_0 \nabla \phi' = 0, \tag{1b}$$

$$\nabla^2 \phi' = 4\pi G \rho'. \tag{1c}$$

$\boldsymbol{u}$ is the displacement vector. $\boldsymbol{\sigma}'$ is the incremental material stress tensor, and ρ' and ϕ' are the incremental local density and gravitational potential, respectively—with the latest including both the tidal potential and the potential arising from the deformation of the body. $\chi = \nabla \cdot \boldsymbol{u}$ is the divergence of the displacement vector, $\boldsymbol{e}_r$ is the radial vector, and g the gravity of the unperturbed body.

To close the system, a constitutive equation relating stress and displacements is required. For an elastic body, we have

$$\boldsymbol{\sigma}' = \lambda \chi \boldsymbol{I} + \mu(\nabla \boldsymbol{u} + (\nabla \boldsymbol{u})^\dagger), \tag{2}$$

where $\dagger$ indicates transpose and $\boldsymbol{I}$ is the identity matrix. λ is the second Lamé parameter ($\lambda = \kappa - \frac{2}{3}\mu$), and μ and κ are the shear and bulk modulus. If the body is viscoelastic, the correspondence principle can be used to relate stress and displacement (e.g., Peltier 1974; Sabadini et al. 2016). Equation (2) still holds, but now μ and λ are the Fourier-transformed shear modulus and Lamé parameter $\hat{\mu}$, $\hat{\lambda}$. For Maxwellian rheology, we have:

$$\hat{\mu}^{-1} = \frac{1}{\mu}\left[1 - \frac{\mathrm{i}}{\omega \tau_M}\right] \tag{3a}$$

$$\hat{\lambda} = \kappa - \frac{2}{3}\hat{\mu}, \tag{3b}$$

where ω is the forcing frequency and τ_M is the Maxwell time $\tau_M = \eta/\mu$, with η being the viscosity. Different expressions for the Fourier-transformed shear modulus and Lamé parameter can be obtained for other rheological models (e.g., Andrade, Voigt-Kelvin, Burgers, Sundberg-Cooper) (Renaud & Henning 2018).

The tidal response is obtained by solving Equations (1) and (2) for a given tidal load, interior structure, and boundary conditions.

2.2. Interior Structure and Model Assumptions

We consider a layered interior. For each layer, the interior properties remain constant with radius. Each layer is characterized by its outer radius, R_i, its density, ρ_i, and its mechanical properties. The mechanical properties (i.e., shear modulus, bulk modulus, and viscosity) are written as mean values (μ_0, κ_0, and η_0) and lateral variations

$$(\mu(r, \theta, \varphi), \kappa(r, \theta, \varphi), \eta(r, \theta, \varphi))$$
$$= (\mu_0(r), \kappa_0(r), \eta_0(r)) + \sum_{n \neq 0, m} (\mu_0 \mu_n^m(r), \kappa_0 \kappa_n^m(r), \eta_0 \eta_n^m(r)) Y_n^m(\theta, \varphi). \tag{4}$$

Y_n^m are spherical harmonics of degree n and order m (see Appendix A.2), and θ and φ are the colatitude and longitude, respectively.

As in previous work (e.g., Qin et al. 2016), we account for the effect of thickness variations ΔH of a layer using using effective shear modulus variations: $\Delta\mu/\mu_0 = \Delta H/H_0$ (e.g., Qin et al. 2016). Yet this is an approximation that deserves further comment. The tidal response of a body whose outer layer is a thin solid shell floating above a liquid layer (i.e., thin-shell body) is controlled by the extension and the bending rigidity: $2(1 + \nu) \mu H$ and $\mu H^3/6(1 - \nu)$ (Beuthe 2018). The effect of shear modulus and shell-thickness variations in the extension rigidity is equivalent. However, this is not true for the bending rigidity. Bending effects are small, provided $(H/R)^2 \ll 1$ and the response has a characteristic long wavelength; when this is the case, they can be neglected (membrane approximation). As bending effects

Table 1
Representative Values for the Nondimensional Parameters for Some Solar System Bodies

Parameter	Definition	Moon	Mercury	Io	Europa	Ganymede	Enceladus
μ_{eff}	$\mu_0/g_s \bar{\rho} R$	6.38	1.22	5.20	0.54	0.45	71.70
r_R	R_2/R	0.22	0.80	0.53	0.98	0.95	0.91
r_ρ	$\rho_3/\bar{\rho}$	0.98	0.54	0.92	0.33	0.52	0.62
$r_{\Delta\rho}$	$(\rho_2 - \rho_3)/\bar{\rho}$	1.60	0.65	0.54	0	0	0
ν	$\frac{3\kappa_0 - 2\mu_0}{6\kappa_0 + 2\mu_0}$	0.36	0.36	0.36	0.33	0.33	0.33
τ	$\omega\eta_0/\mu_0$	⋯	⋯	3.42	⋯	0	⋯
μ_n^m, $\Delta\mu/\mu_0$ ($\Delta H/H_0$)	Equation (4)	⋯	⋯	0.1	0.2	⋯	1
κ_n^m, $\Delta\kappa/\kappa_0$	Equation (4)	⋯	⋯	⋯	⋯	⋯	⋯
η_n^m, $\Delta\eta/\eta_0$	Equation (4)	⋯	⋯	1	⋯	⋯	⋯
k_2^u	Equation (28)	0.025	0.44	0.056 − 0.0150i	0.23	0.4	0.016
h_2^u	Equation (28)	0.042	0.8	0.1 − 0.026i	1.16	1.3	0.044

Notes. The shear and bulk modulus of ice and rock are from Souček et al. (2019) and Kervazo et al. (2021), respectively. For the Moon, we consider a core radius of 390 km and adjust the core and mantle densities to meet the density density and *MoI* constraint. For Mercury, the interior structure follows from the average density, and the total and outer shell moments of inertia (Genova et al. 2019). Io's interior model is from Steinke et al. (2020a). Ice shell-thickness values for Europa, Ganymede, and Enceladus are from Hussmann et al. (2002), Beuthe et al. (2016), and Vance et al. (2018). We assume ice and ocean densities of 1000 kg.m^{-3}, and the core density is set to meet the mean density constraint. Io's viscosity is adjusted to match the $\Im(k_2)$ from astrometric observations (Lainey et al. 2009). Lateral variations are given in terms of maximum peak-to-peak variations with respect to the mean value. For Io, representative viscosity and shear modulus variations follow from expected variations in tidal heating (Steinke 2021); for Enceladus and Europa, expected shell-thickness variations are from Beuthe et al. (2016) and Nimmo et al. (2007), respectively. The gravitational and radial displacement Love numbers (k_2^u and h_2^u) for the spherically symmetric elastic case are also given.

become more relevant (e.g., thicker outer shells and shorter wavelength), the use of an effective shear modulus to mimic thickness variations becomes less accurate. Beuthe (2018) applied thin-shell theory to study the deformation of Enceladus with lateral shell-thickness variations, and showed that the membrane approximation renders good results, provided shell variations are of long wavelength. As bending effects are expected to be smaller in larger icy moons (e.g., Europa and Ganymede), we expect this approximation to hold better for these moons.

While the method described below can be applied to any layered interior structure, we will consider a simplified three-layer model consisting of a nondeformable solid core of density ρ_1 surrounded by an incomprehensible liquid layer in hydrostatic equilibrium with outer radius R_2 and density ρ_2; and a solid shell with outer radius R, density ρ_3, and mean shear modulus, bulk modulus, and viscosity μ_0, κ_0, and η_0. This simple model can be used to represent rocky and icy bodies. For the former, the innermost two layers correspond to the inner and the outer core, and the outermost layer represents both the rocky mantle and crust. For the latter, the core corresponds to the rocky core, the liquid layer to a subsurface ocean, and the outer layer to the ice shell. This simplified model neglects the gravitational coupling between the inner solid core and the surrounding shell, which typically have a small effect on the tidal response, as well as dynamic liquid tides in the liquid layer, which under certain circumstances can play a relevant role in the tidal response (e.g., Rovira-Navarro et al. 2019, 2023).

The tidal response is controlled by a set of nondimensional parameters. The tidal response of an incompressible homogeneous elastic body only depends on the effective rigidity μ_{eff}. A body with high effective rigidity exhibits small tidal deformations. The role of compressibility depends on the Poisson's ratio ν. For $\nu \approx 0.5$, the body behaves as an incompressible body. Viscous effects depend on the nondimensional Maxwell time τ. Bodies with $\tau \to \infty$ behave elastically. The introduction of a solid core and a liquid layer

adds three nondimensional parameters: the ratio between the outer radius of the liquid layer and surface radius, r_R; the ratio between the outer layer density and the mean density, r_ρ; and the density contrast between the liquid and solid shells, $r_{\Delta\rho}$. For icy moons with subsurface oceans, $r_{\Delta\rho} \approx 0$, while for rocky worlds, we will assume that the inner and outer core have the same density. Lateral rheology variations introduce additional nondimensional parameters. The effect of lateral variations of rheology properties depend on the parameters κ_n^m, μ_n^m, and η_n^m. Characteristic nondimensional parameters for tidally active Solar System bodies are listed in Table 1.

3. Spectral Method

Different approaches can be used to solve Equation (1). We use a spectral method that employs tensor spherical harmonics as basis functions (James & Cook 1976). The properties of spherical harmonics allow to transform the three-dimensional governing equations into a set of partial differential equations that depend only on radial distance. In this section, we describe the new spectral method. First, we explain how the different fields are expanded using tensor spherical harmonics (Section 3.1); we then provide the governing equations and boundary conditions in the spectral domain (Sections 3.2 and 3.3); finally, we extend the definition of Love numbers traditionally used for spherically symmetric bodies to laterally heterogeneous bodies and obtain expressions to compute tidal energy dissipation for the anelastic case (Sections 3.4 and 3.5). The appendices contain further details about the method. Appendix A provides definitions of tensor spherical harmonics; Appendix B gives explicit expressions to compute various integrals of products of tensor spherical harmonics required for this approach; and Appendix C provides explicit expressions for the governing equations.

3.1. Spectral Expansion

As we are considering a periodic forcing, it is convenient to work in the Fourier domain. The tidal potential, ϕ^T, can be

written as

$$\phi^T(r, \theta, \varphi, t) = \sum_k \left(\frac{r}{R}\right)^{n_k} \phi^{(T)}{}_{n_k}^{m_k,\omega_k} Y_{n_k}^{m_k}(\theta, \varphi) e^{i\omega_k t}. \quad (5)$$

n_k, m_k, and ω_k are respectively the degree, order, and frequency of the tidal force. ϕ^T should be real, implying that for each n_k, m_k, $+\omega$ component there is an n_k, $-m_k$, $-\omega$ component with amplitude $\phi^{(T)}{}_{n_k}^{-m_k,-\omega_k} = (-1)^m \overline{\phi^{(T)}{}_{n_k}^{m_k,\omega_k}}$, where $-$ indicates the complex conjugate. The amplitude of $\phi^{(T)}{}_{n_k}^{m_k,\omega_k}$ depends on the tidal component considered—Appendix D provides the expression corresponding to a synchronous satellite in an eccentric orbit. As Equation (1) is linear, the complete tidal response can be obtained by linearly adding the solution for each tidal component. In what follows, we will consider the solution to a tidal force of frequency ω of the form

$$\phi^T(r, \theta, \varphi, t) = \left(\frac{r}{R}\right)^{n_T} (\phi^{(T)}{}_{n_T}^{m_T,+} Y_{n_T}^{m_T}(\theta, \varphi) e^{i\omega t}$$
$$+ (-1)^{m_T} \overline{\phi^{(T)}{}_{n_T}^{m_T,+}} Y_{n_T}^{-m_T}(\theta, \varphi) e^{-i\omega t}). \quad (6)$$

The $+$ and $-$ components correspond to the $+\omega$ and $-\omega$ components of the tidal force.

We expand rank 0 tensors, such as the perturbing potential ϕ' and the divergence of the displacement vector $\nabla \cdot \boldsymbol{u}$, using spherical harmonics of rank 0:

$$(\phi'(r, \theta, \varphi, t), \chi(r, \theta, \varphi, t)) = \sum_{n,m}[(\phi_n^{m,+}(r), \chi_n^{m,+}(r)) e^{i\omega t}$$
$$+ (\phi_n^{m,-}(r), \chi_n^{m,-}(r)) e^{-i\omega t}] Y_n^m(\theta, \varphi),$$
$$(7)$$

where summation is over $n \in [0, \infty]$ and $m \in [-n, n]$.

The rheology parameters are also expanded in spherical harmonics (Equation (4)). For an anelastic body, the complex shear modulus is obtained using the correspondence principle (Equation (3)),

$$\hat{\mu}(r, \theta, \varphi) = \mu_0(r)\left(1 + \sum_{n\neq 0,m} \mu_n^m(r) Y_n^m(\theta, \varphi)\right)$$

$$\times \left(1 - \frac{i}{\omega \tau_{M,0}(r)} \frac{1 + \sum_{n\neq 0,m}\mu_n^m(r) Y_n^m(\theta, \varphi)}{1 + \sum_{n\neq 0,m}\eta_n^m(r) Y_n^m(\theta, \varphi)}\right)^{-1}, \quad (8)$$

with $\tau_{M,0} = \eta_0/\mu_0$ being the average Maxwell time. The Fourier-transformed shear modulus can be decomposed into spherical harmonics:

$$\hat{\mu}(r, \theta, \varphi) = \hat{\mu}_0(r) + \mu_0 \sum_{n\neq 0,m} \hat{\mu}_n^m(r) Y_n^m(\theta, \varphi), \quad (9)$$

with

$$(\mathfrak{R}(\hat{\mu}_n^m), \mathfrak{I}(\hat{\mu}_n^m)) = \frac{1}{4\pi\mu_0} \int_\Omega (\mathfrak{R}(\hat{\mu}), \mathfrak{I}(\hat{\mu})) \overline{Y_n^m} d\Omega. \quad (10)$$

$\mathfrak{R}$ and $\mathfrak{I}$ denote the real and imaginary components, respectively. For an elastic body, we have $\hat{\mu}_0 = \mu_0$ and $\hat{\mu}_n^m = (-1)^m \overline{\hat{\mu}_n^{-m}}$.

The displacement vector is expanded using tensor spherical harmonics of rank 1 (Appendix A.3):

$$\boldsymbol{u}(r, \theta, \varphi, t) = \sum_{n,n_1,m} [u_{n,n_1}^{m,+}(r) e^{i\omega t} + u_{n,n_1}^{m,-}(r) e^{-i\omega t}] \boldsymbol{Y}_{n,n_1}^m(\theta, \varphi),$$
$$(11)$$

where summation is over $n \in [0, \infty]$, $m \in (-n, n)$, and $n_1 \in [n-1, n+1]$. The decomposition in tensor spherical harmonics automatically separates between spheroidal ($n_1 = n \pm 1$) and toroidal components $n_1 = n$. This expansion is different from that traditionally used to solve the viscoelastic-gravitational problem, which uses the radial-poloidal-toroidal decomposition:

$$\boldsymbol{u}(r, \theta, \varphi, t) = \sum_{n,m} (U_n^{m,+}(r) \boldsymbol{R}_n^m(\theta, \varphi)$$
$$+ V_n^{m,+}(r) \boldsymbol{S}_n^m(\theta, \varphi) + W_n^{m,+}(r) \boldsymbol{T}_n^m(\theta, \varphi)) e^{i\omega t} + c.c, \quad (12)$$

where $c.c$ means complex conjugate. U_n^m, V_n^m, W_n^m and $u_{n,n-1}^m$, $u_{n,n}^m$, $u_{n,n+1}^m$ are related via a linear transformation (Equation (A14)).

The stress and strain tensors are expanded using tensor spherical harmonics of rank 2 (Appendix A.4):

$$(\boldsymbol{\sigma}'(r, \theta, \varphi, t), \boldsymbol{\epsilon}'(r, \theta, \varphi, t))$$
$$= \sum_{\substack{n,n_1,\\n_2,m}} [(\sigma_{n,n_1,n_2}^{m,+}(r), \epsilon_{n,n_1,n_2}^{m,+}(r)) e^{i\omega t}$$
$$+ (\sigma_{n,n_1,n_2}^{m,-}(r), \epsilon_{n,n_1,n_2}^{m,-}(r)) e^{-i\omega t}] \boldsymbol{Y}_{n,n_1,n_2}^m(\theta, \varphi), \quad (13)$$

where summation is over $n \in [0, \infty]$, $m \in [-n, n]$, $n_1 \in [n-1, n+1]$, and $n_2 \in [n_1-1, n_1+1]$. Generally, rank 2 tensors have nine independent components, but as the stress and strain tensors are symmetric, they only have six independent components. Because of this, it is convenient to use an alternative projection based on tensor harmonics defined by Zerilli (Zerilli 1970). Following the notation of James & Cook (1976),

$$(\boldsymbol{\sigma}'(r, \theta, \varphi, t), \boldsymbol{\epsilon}'(r, \theta, \varphi, t))$$
$$= \sum_{n,n_2,m,l} [(\sigma_{n,n_2;m}^{(l),+}(r), \epsilon_{n,n_2;m}^{(l),+}(r)) e^{i\omega t}$$
$$+ (\sigma_{n,n_2;m}^{(l),-}(r), \epsilon_{n,n_2;m}^{(l),-}(r)) e^{-i\omega t}] \boldsymbol{T}_{n,n_2;m}^{(l)}(\theta, \varphi). \quad (14)$$

This projection has the advantage of separating the trace $l = 0$, anti-symmetric $l = 1$, and symmetric trace-free $l = 2$ components. For a symmetric rank 2 tensor, there are six nonzero components of the stress and strain tensor for each degree and order: the trace ($l = 0$, $n_2 = 0$) and the symmetric spheroidal ($l = 2$, $n_2 = n$ and $n_2 = n \pm 2$) and toroidal ($l = 2$, $n_2 = n \pm 1$) components. The Zerilli and rank 2 spherical harmonics tensor spherical harmonics are linearly related (see Appendix A.4).

To apply the boundary conditions, the radial components of the stress tensor are required. The radial component of the stress tensor can be written in the rank 1 spherical harmonics basis or alternatively in the radial-poloidal-toroidal basis often

used in the literature:

$$
\begin{aligned}
\boldsymbol{e}_r \cdot \boldsymbol{\sigma}' = \sum_{n,m} [& R_n^{m,+}(r)\boldsymbol{R}_n^m(\theta, \varphi) + S_n^m(r)\boldsymbol{S}_n^{m,+}(\theta, \varphi) \\
& + T_n^{m,+}(r)\boldsymbol{T}_n^m(\theta, \varphi)]\mathrm{e}^{\mathrm{i}\omega t} + c.c.
\end{aligned}
\tag{15}
$$

The spheroidal, poloidal, and toroidal components can be written in terms of the $\sigma_{n,n_2;m}^{(l)}$ components of the stress tensor (Equation (C9)).

The previous tensors must be real, which implies that the $+$ and $-$ components are related. Once the solution to the $+$ component is obtained, the solution to the $-$ component follows immediately from the complex-conjugate properties of tensor spherical harmonics (see Appendix A.1)

3.2. Spectral Form of the Governing Equations

Using the spectral expansions defined in Section 3.1 and the properties of tensor spherical harmonics (James & Cook 1976), we can transform the mass and momentum conservation equations and Poisson equation (Equation (1)) as well as the constitutive law (Equation (2)) to the spectral domain.

The components of the momentum equations (Equation (1b)) in the $\boldsymbol{Y}_{n,n-1}^m$, $\boldsymbol{Y}_{n,n}^m$, and $\boldsymbol{Y}_{n,n+1}^m$ bases are given by

$$
\begin{aligned}
& \sum_{n_2,l}(-1)^{n+n_2}\Lambda(n_1, l)\begin{Bmatrix} 1 & l & 1 \\ n & n_1 & n_2 \end{Bmatrix} \\
& \times G(n_1, n_2)\partial_{n_2}^{n_1}\sigma_{n,n_2;m}^{(l)} - \rho_0 G(n, n_1) \\
& \sum_{n_{1\alpha}} G(n, n_{1\alpha})\partial_n^{n_{1\alpha}}(gu_{n,n_{1\alpha}}^m) \\
& -g\rho_0 G(n, n_1)\chi_n^m - \rho_0 G(n, n_1)\partial_n^{n_1}\phi_n^m = 0,
\end{aligned}
\tag{16}
$$

with $n_1 \in [n-1, n+1]$. Here, $G(n, n_1)$, $\partial_{n_1}^{n_2}$, and $\Lambda(n_1, l)$ are operators defined in Equations (A19) and (A3); and the terms between curly brackets are Wigner's 6-j symbols.

The Poisson equation (Equation (1c)) is

$$
D_n\phi_n^m = -4\pi G\rho\chi_n^m - 4\pi G\partial_r\rho_0 \sum_{n_{1\alpha}} G(n, n_{1\alpha})u_{n,n_{1\alpha}}^m,
\tag{17}
$$

where ∂_r stands for the derivative with respect to the radial distance r, and D_n is an operator defined in Equation (A20). The right-hand side is 0 if the density is uniform within the layer and the solid is incompressible. The explicit forms of the momentum and the Poisson equation are given in Appendix C.

To obtain the spectral form of the constitutive law (Equation (2)), it is useful to rewrite it as

$$
\begin{aligned}
\boldsymbol{\sigma}' &= (3\lambda + 2\mu)\boldsymbol{T}(\nabla\boldsymbol{u}) + 2\mu\boldsymbol{S}(\nabla\boldsymbol{u}) \\
&= (3\lambda + 2\mu)\boldsymbol{T}(\boldsymbol{\epsilon}') + 2\mu\boldsymbol{S}(\boldsymbol{\epsilon}').
\end{aligned}
\tag{18}
$$

$\boldsymbol{T}$ and $\boldsymbol{S}$ stand for the trace and trace-free symmetric parts of the tensor, and we have used the following definition of the strain tensor:

$$
\boldsymbol{\epsilon}' = \frac{1}{2}(\nabla\boldsymbol{u} + (\nabla\boldsymbol{u})^\dagger) = \boldsymbol{T}(\nabla\boldsymbol{u}) + \boldsymbol{S}(\nabla\boldsymbol{u}).
\tag{19}
$$

An explicit expression for the strain tensor, which can be obtained using the properties listed in Section 3 of James & Cook (1976), is given in Appendix C.

Plugging Equation (4) into Equation (18) and using the spectral expansion of the strain tensor, we can obtain the stress tensor as

$$
\boldsymbol{\sigma}' = \left(\hat{A}_0 + A_0 \sum_{n_\beta,m_\beta} \hat{A}_{n_\beta}^{m_\beta} Y_{n_\beta}^{m_\beta}\right)\left(\sum_{\substack{n_\alpha,n_{2\alpha}, \\ l_\alpha,m_\alpha}} \epsilon_{n_\alpha,n_{2\alpha};m_\alpha}^{(l_\alpha)}\boldsymbol{T}_{n_\alpha,n_{2\alpha};m_\alpha}^{(l_\alpha)}\right),
\tag{20}
$$

with

$$
\hat{A} = \begin{cases} 3\kappa, & \text{if } l = 0 \\ 2\hat{\mu}, & \text{if } l = 2 \end{cases}.
\tag{21}
$$

$\hat{A}_0$ and $A_0\hat{A}_n^m$ stand for the laterally uniform and laterally varying components of A, respectively. Finally, the components of the stress tensor $\sigma_{n,n_2;m}^{(l)}$ are obtained by projecting the stress tensor into a basis of Zerilli's tensors,

$$
\sigma_{n,n_2;m}^{(l)} = \frac{1}{4\pi}\int \boldsymbol{\sigma}' : \overline{\boldsymbol{T}_{n,n_2;m}^{(l)}}\mathrm{d}\Omega,
\tag{22}
$$

where $:$ is the inner product. Using Equation (20), we find

$$
\begin{aligned}
\sigma_{n,n_2;m}^{(l)} = \hat{A}_0\,\epsilon_{n,n_2;m}^{(l)} + A_0 \sum_{n_\beta,m_\beta} & \hat{A}_{n_\beta}^{m_\beta} \\
& \sum_{\substack{n_\alpha,n_{2\alpha}, \\ l_\alpha,m_\alpha}} \epsilon_{n_\alpha,n_{2\alpha};m_\alpha}^{(l_\alpha)}(\boldsymbol{T}_{n_\alpha,n_{2\alpha};m_\alpha}^{(l_\alpha)} : \overline{\boldsymbol{T}_{n,n_2;m}^{(l)}} \cdot Y_{n_\beta}^{m_\beta}).
\end{aligned}
\tag{23}
$$

$(\boldsymbol{T}_{n_\alpha,n_{2\alpha};m_\alpha}^{(l_\alpha)} : \overline{\boldsymbol{T}_{n,n_2;m}^{(l)}} \cdot Y_{n_\beta}^{m_\beta})$ are the coupling coefficients, which indicate the coupling of mode (n_α, m_α) and (n,m) due to rheology variations of degree and order (n_β, m_β). The coupling coefficients with nonzero value determine which modes are coupled. Their explicit form and properties are given in Appendix B.

Equations (16), (17), (19), and (23) form a closed set of partial differential equations that can be solved under well-posed boundary conditions.

3.3. Boundary Conditions

To obtain the tidal response, the previous set of equations must be solved under appropriate boundary conditions. We impose boundary conditions at the surface R and at the core–mantle boundary R_2. The derivation of the boundary conditions can be found in Sabadini et al. (2016). At the surface, R, the stress vanishes:

$$
R_n^m = 0 \quad S_n^m = 0, \quad T_n^m = 0,
\tag{24}
$$

and the potential stress, Q, is given by

$$
Q_n^m = \partial_r\phi_n^m + \frac{n+1}{R}\phi_n^m + 4\pi G\rho_3 U_n^m = \frac{2n_T + 1}{R}\delta_{n_T}^n\delta_{m_T}^m,
\tag{25}
$$

with n_T and m_T being the degree and order of the considered tidal forcing.

At the boundary between the liquid layer and the outermost solid layer (R_2), there is zero tangential and zero toroidal stress, and the radial stress is given by the difference between the radial displacement and the geoid:

$$
S_n^m = 0, \quad T_n^m = 0; \quad R_n^m = \rho_2 g\left(U_n^m + \frac{\phi_n^m}{g}\right).
\tag{26}
$$

The gradient of the gravitational potential is

$$\partial_r \phi_n^m = \frac{n}{r}\phi_n^m + \frac{4\pi G}{g\rho_2}(\rho_3 - \rho_2)(\rho_2\phi_n^m - R_n^m). \qquad (27)$$

Degrees 0 and 1 require special treatment (Farrell 1972; Qin et al. 2014). For degree 0, the displacement and radial stress vector only have radial components. Because of compressibility, the body can experience nonzero radial displacements. However, as the mass of the body does not change, the perturbing potential should be 0, $\phi_0 = 0$. The degree 1 solution automatically satisfies $R_1^m + 2S_1^m + \frac{gQ_1^m}{4\pi G} = 0$, which implies that two of the boundary conditions are a linear combination of each other. This is because the degree 1 solution includes a translation of the center of mass that does not introduce stress. As we are working in the center of mass reference center, we constrain this translation to be 0, $\phi_1^m = 0$. Moreover, $T_1^m(R_2) = 0$ is automatically fulfilled if $T_1^m(R) = 0$. This is because the toroidal mode contains a net rotation that does not introduce stress. Instead of using $T_n^m(R_2) = 0$, we impose a 0 toroidal displacement at R_2 without introducing extra stress $W_1^m(R_2) = 0$, as done in Qin et al. (2014).

3.4. Love Numbers of an Aspherical Body

The tidal response of a body can be expressed in terms of Love numbers, a set of dimensionless proportionality constants that relate the tidal force and the body's response. For a spherically symmetric body, a tidal forcing of a given degree and order results in a response of the same degree and order. Moreover, due to the spherical symmetry, the Love numbers are independent of the order of the forcing. Because of this, there exist a set of frequency-dependent Love numbers (radial h_n, poloidal l_n, and gravitational k_n) per degree that can be evaluated at any radial point. If there are lateral heterogeneities, a forcing of a given wavelength might excite a mode with different wavelength. Because of this, the definition of Love numbers must be extended. More generally, we can write the tidal response as

$$(U, V, W, \phi) = \sum_{n_\alpha, m_\alpha} \sum_{n_\beta, m_\beta} \left(-\frac{h_{n_\alpha, m_\alpha}^{n_\beta, m_\beta}}{g_0}, \right.$$
$$-\frac{l_{n_\alpha, m_\alpha}^{n_\beta, m_\beta}}{g_0}, -\frac{t_{n_\alpha, m_\alpha}^{n_\beta, m_\beta}}{g_0}, \delta_{n_\alpha}^{n_\beta}\delta_{m_\alpha}^{m_\beta}$$
$$\left. +k_{n_\alpha, m_\alpha}^{n_\beta, m_\beta} \right)\phi^{(T)\,m_\alpha,+}_{n_\alpha}Y_{n_\beta}^{m_\beta}e^{i\omega t} + c.c. \qquad (28)$$

α and β indicate the tidal response at degree and order n_β, m_β due to a forcing at degree and order n_α, m_α. t are the toroidal Love number, which are 0 for a spherically symmetric body. The only nonzero numbers Love numbers for a spherically symmetric body are $h_{n_\alpha, m_\alpha}^{n_\alpha, m_\alpha}$, $l_{n_\alpha, m_\alpha}^{n_\alpha, m_\alpha}$, $k_{n_\alpha, m_\alpha}^{n_\alpha, m_\alpha}$, and as they are independent of order, they can be simply written as h_n, l_n, and k_n.

3.5. Energy Dissipation

If the body is anelastic, its deformation is not adiabatic. The mean volumetric energy dissipated during a tidal period T is given by

$$\dot{e}(r, \theta, \varphi) = \frac{1}{T}\int_t^{t+T} \boldsymbol{\sigma}'(r, \theta, \varphi, t) : \dot{\boldsymbol{\epsilon}}'(r, \theta, \varphi, t)\mathrm{d}t. \qquad (29)$$

The previous integral can be computed either in the temporal–spatial domain using $\epsilon(t, r, \theta, \varphi)$ and $\sigma(t, r, \theta, \varphi)$, or alternatively in the spectral domain using their spectral expansions. Plugging Equation (14) into Equation (29) and performing the time integral, we find

$$\dot{e} = \omega i \sum_{\substack{n_\alpha, n_{2\alpha}, l_\alpha \\ n_\beta, n_{2\beta}, l_\beta\, m_\alpha, m_\beta}} \boldsymbol{T}_{n_\alpha, n_{2\alpha}; m_\alpha}^{(l_\alpha)} : \boldsymbol{T}_{n_\beta, n_{2\beta}; m_\beta}^{(l_\beta)}$$
$$(\sigma_{n_\alpha, n_{2\alpha}; m_\alpha}^{(l_\alpha), -}\epsilon_{n_\beta, n_{2\beta}; m_\beta}^{(l_\beta), +} - \sigma_{n_\alpha, n_{2\alpha}; m_\alpha}^{(l_\alpha), +}\epsilon_{n_\beta, n_{2\beta}; m_\beta}^{(l_\beta), -}). \qquad (30)$$

For a given radius, we can project the previous expression into spherical harmonics to obtain the spectra of energy dissipation, i.e.,

$$\dot{e}(r, \theta, \varphi) = \sum_{n, m} e_n^m(r)Y_n^m(\theta, \varphi), \qquad (31)$$

with

$$\dot{e}_{n_\nu}^{m_\nu}(r) = \omega i \sum_{\substack{n_\alpha, n_{2\alpha}, l_\alpha \\ n_\beta, n_{2\beta}, l_\beta\, m_\alpha, m_\beta}} (\sigma_{n_\alpha, n_{2\alpha}; m_\alpha}^{(l_\alpha), -}\epsilon_{n_\beta, n_{2\beta}; m_\beta}^{(l_\beta), +}$$
$$-\sigma_{n_\alpha, n_{2\alpha}; m_\alpha}^{(l_\alpha), +}\epsilon_{n_\beta, n_{2\beta}; m_\beta}^{(l_\beta), -})(\boldsymbol{T}_{n_\alpha, n_{2\alpha}; m_\alpha}^{(l_\alpha)} : \boldsymbol{T}_{n_\beta, n_{2\beta}; m_\beta}^{(l_\beta)} \cdot \overline{Y_{n_\nu}^{m_\nu}}). \qquad (32)$$

$(\boldsymbol{T}_{n_\alpha, n_{2\alpha}; m_\alpha}^{(l_\alpha)} : \boldsymbol{T}_{n_\beta, n_{2\beta}; m_\beta}^{(l_\beta)} \overline{Y_{n_\nu}^{m_\nu}})$ is an integral defined in Appendix B. The average energy dissipation for radius r is given by $\dot{e}_0^0(r)$ and can be obtained using the orthogonality and complex-conjugate properties of tensor spherical harmonics (Appendix A.1):

$$\dot{e}_0^0(r) = 2\omega \sum_{n, n_2, l, m} [\Im(\sigma_{n, n_2, l}^{m, +})\Re(\epsilon_{n, n_2, l}^{m, +})$$
$$-\Re(\sigma_{n, n_2, l}^{m, +})\Im(\epsilon_{n, n_2, l}^{m, +})]. \qquad (33)$$

The total energy dissipation can be found by radially integrating $\dot{e}_0^0$,

$$\dot{E} = \int_V \dot{e}\mathrm{d}V = \int_S \int_{r_1}^{r_2} \sum_{n, m} \dot{e}_n^m(r)Y_n^m r^2\mathrm{d}\Omega\mathrm{d}r$$
$$= 4\pi \int_{r_1}^{r_2} \dot{e}_0^0(r)r^2\mathrm{d}r. \qquad (34)$$

Alternatively, the total tidal dissipation can be obtained from the work done by the tidal force (Love 1927),

$$\dot{E} = \frac{1}{T}\int_V \int_T \rho\frac{\partial\boldsymbol{u}}{\partial t} \cdot \nabla\phi^T\mathrm{d}t\mathrm{d}V, \qquad (35)$$

which can be transformed into a surface integral (e.g., Peale & Cassen 1978; Zschau 1978; Platzman 1984),

$$\dot{E} = \frac{\omega}{8\pi^2 GR}\sum_n (2n + 1)\int_T \int_S \phi_n^T\frac{\partial\phi'_n}{\partial t}\mathrm{d}t\mathrm{d}S, \qquad (36)$$

where ϕ' is the perturbing potential (i.e., $\phi = \phi' + \phi^T$) and the subscript n indicates that only the component of degree n of the potential is considered. Using the spectral expansion of the tidal potential (Equation (5)), the definition of the Love numbers (Equation (28)) and the orthogonality of spherical

harmonics, we find:

$$\dot{E} = -2\frac{\omega R}{G} \sum_{\substack{n_1,m_1, \\ n_2,m_2}} (2n+1)\phi^{(T)}{}_{n_1}^{m_1,+}\phi^{(T)}{}_{n_2}^{m_2,+}\mathfrak{J}(k_{n_2,m_2}^{n_1,m_1}). \quad (37)$$

If we consider a spherically symmetric body in an eccentric orbit, the previous expression reduces to the classic expression (e.g., Peale et al. 1979):

$$\dot{E} = -\frac{21}{2}\frac{(\omega R)^5 e^2}{G}\mathfrak{J}(k_2). \quad (38)$$

4. Numerical Approach

The system of differential equations presented in Section 3.2 is written in terms of the three components of the displacement vector ($u_{n,n-1}^m$, $u_{n,n}^m$, $u_{n,n+1}^m$), the six components of the strain ($\epsilon_{n,n;m}^{(0)}$, $\epsilon_{n,n-2;m}^{(2)}$, $\epsilon_{n,n-1;m}^{(2)}$, $\epsilon_{n,n;m}^{(2)}$, $\epsilon_{n,n+1;m}^{(2)}$, $\epsilon_{n,n+2;m}^{(2)}$) and stress ($\sigma_{n,n;m}^{(0)}$, $\sigma_{n,n-2;m}^{(2)}$, $\sigma_{n,n-1;m}^{(2)}$, $\sigma_{n,n;m}^{(2)}$, $\sigma_{n,n+1;m}^{(2)}$, $\sigma_{n,n+2;m}^{(2)}$) tensors, and the gravitational potential (ϕ_n^m), for each degree and order. However, it is more convenient to rewrite the equations in terms of the variables traditionally employed to solve the viscoelastic deformation of a self-gravitating body (e.g., Love 1911; Farrell 1972; Sabadini et al. 2016): the radial, poloidal, and toroidal components of the displacement vector and of the radial component of the stress tensor (U_n^m, V_n^m, W_n^m, R_n^m, S_n^m, T_n^m) and the gravitational potential and its gradient (ϕ, $\partial_r\phi$):

$$\begin{aligned}
\boldsymbol{y} &= (U_0, R_0, \phi_0, \partial_r\phi_0, \dots U_n^m, \\
&V_n^m, R_n^m, S_n^m, \phi_n^m, \partial_r\phi_n^m, W_n^m, T_n^m \dots U_\infty^\infty, \\
&V_\infty^\infty, R_\infty^\infty, S_\infty^\infty, \phi_\infty^\infty, \partial_r\phi_\infty^\infty, W_\infty^\infty, T_\infty^\infty) \\
&= (y_{0,1}, y_{0,3}, y_{0,5}, y_{0,6}, \dots y_{n,1}^m, y_{n,2}^m, y_{n,3}^m, y_{n,4}^m, y_{n,5}^m, y_{n,6}^m, y_{n,7}^m \\
&y_{n,8}^m \dots y_{\infty,1}^\infty, y_{\infty,2}^\infty, y_{\infty,3}^\infty, y_{\infty,4}^\infty, y_{\infty,5}^\infty, y_{\infty,6}^\infty, y_{\infty,7}^\infty, y_{\infty,8}^\infty),
\end{aligned} \quad (39)$$

where we have also introduced the y radial functions traditionally used in the viscoelastic–gravitational problem (e.g., Sabadini et al. 2016). We note that the problem is formulated in terms of the gradient of the gravitational potential $y_6 = \partial_r\phi$ rather than the potential stress Q. The equations can be then be cast in the form (Appendix C)

$$\partial_r\boldsymbol{y}(r) = \boldsymbol{D}\boldsymbol{y}(r), \quad (40)$$

where $\boldsymbol{D}$ is a linear operator that depends on the interior properties and the radial distance r.

Given a forcing of degree n_T and order m_T, not all the modes (n, m) are excited. If there are no lateral rheology variations, equations of different degree and order are decoupled. Additionally, if we only consider a zonal forcing $m_T=0$ and no longitudinal rheology variations (i.e., $\kappa_n^m = \mu_n^m = \eta_n^m = 0$ for $m \neq 0$), spheroidal (U_n^m, V_n^m, R_n^m, S_n^m, ϕ_n^m, $\partial_r\phi_n^m$) and toroidal (W_n^m, T_n^m) modes are decoupled. More generally, the modes (n,m) involved in the tidal response depend on the forcing spectra (n_T, m_T) and that of the lateral variations (n_{LV}, m_{LV}) via the coupling terms. Given a mode (n_α, m_α) and lateral variations of the form (n_{LV}, m_{LV}), the coupled modes (n_α, m_α) $\otimes$ (n_{LV}, m_{LV}) $\Rightarrow$ (n, m) are given by the nonzero coupling coefficients. The coupled modes can be obtained recursively by using the selection rules listed in Appendix B. Starting from the tidal force (n_T, m_T), the modes involved in the solution can be obtained by recursively applying the selection rules: first-order modes, (n_T, m_T) $\otimes$ (n_{LV}, m_{LV}) $\Rightarrow$ (n_1, m_1), second-order modes (n_1, m_1) $\otimes$ (n_{LV}, m_{LV}) $\Rightarrow$ (n_2, m_2), and modes of order p, (n_{p-1}, m_{p-1}) $\otimes$ (n_{LV}, m_{LV}) $\Rightarrow$ (n_p, m_p).

As opposed to a spherically symmetric body, for which there is only one mode involved in the tidal response per forcing harmonic (n_T, m_T), an infinite set of modes are excited by the tidal force when lateral variations are considered. This makes it impossible to obtain an exact solution to the problem using the spectral method. An approximate solution is obtained by setting a maximum cutoff order N_p. The reduced system of differential equations is given by

$$\partial_r\boldsymbol{y}_a(r) = \boldsymbol{D}_a\boldsymbol{y}_a(r), \quad (41)$$

with $\boldsymbol{y}_a$ containing only the considered modes and $\boldsymbol{D}_a$ their corresponding dynamics. $\boldsymbol{y}_a$ is an $8N_{\text{modes}}$ vector or $8(N_{\text{modes}} - 1) + 4$ vector if the degree 0 response is excited. To obtain the tidal response, Equation (41) is integrated numerically from the boundary between the liquid layer and the outermost solid layer (R_2) to the surface using a Runge–Kutta scheme. The solution is given by

$$\boldsymbol{y}_a = \sum_{n,m,k} C_{n,k}^m \boldsymbol{y}_{n,k}^m. \quad (42)$$

$C_{n,k}^m$ are a set of $8N_{\text{modes}}$, or $8(N_{\text{modes}} - 1) + 4$ if the degree 0 is excited, integration constants; and $\boldsymbol{y}_{n,k}^m$ are the corresponding set of solution vectors with $y_{n',k'}^{m'}(R_2) = \delta_n^{n'}\delta_m^{m'}\delta_k^{k'}$.

The integration constants are obtained by applying the boundary conditions listed in Section 3.3, and the solution follows from Equation (42). Once the radial functions y are obtained, the components of the displacement vector, and strain and stress tensors in tensor spherical harmonic bases are obtained using Equations (A14), (C1), and (C4). The solution can be transformed from the spectral domain to the spatial and time domain using Equations (7), (11), and (14), and the definitions of the rank 0 (Equation (A9)), rank 1 (Equation (A11)), and rank 2 (Equation (A16)) tensor spherical harmonics.

Figure 1 provides an overview of the method described above, which is implemented in the *LOV3D* software repository.

5. Model Benchmark and Comparison with Previous Methods

We compare the results obtained with the spectral method presented here with those obtained using the spectral-perturbation method of Qin et al. (2014, 2016) and the FEM code of Berne et al. (2023a, 2023b).

The spectral method of Qin et al. (2014, 2016) relies on perturbation theory. As opposed to the method presented above, the solution is computed recursively. The tidal response of the spherically symmetric body is used to obtain the first-order modes which is then employed to compute second-order modes, etc. For each mode, only the radial functions corresponding to that mode are considered unknown. The coupling terms (second term in the RHS of Equation (23), and terms related to lateral variations in Equation (C11)) are considered to be known and follow from a lower-order mode, effectively acting as a forcing. This way, the equations corresponding to each of the modes participating in the tidal response are decoupled. This means that, for a mode of a given perturbation order, the effect of higher-order modes is ignored.
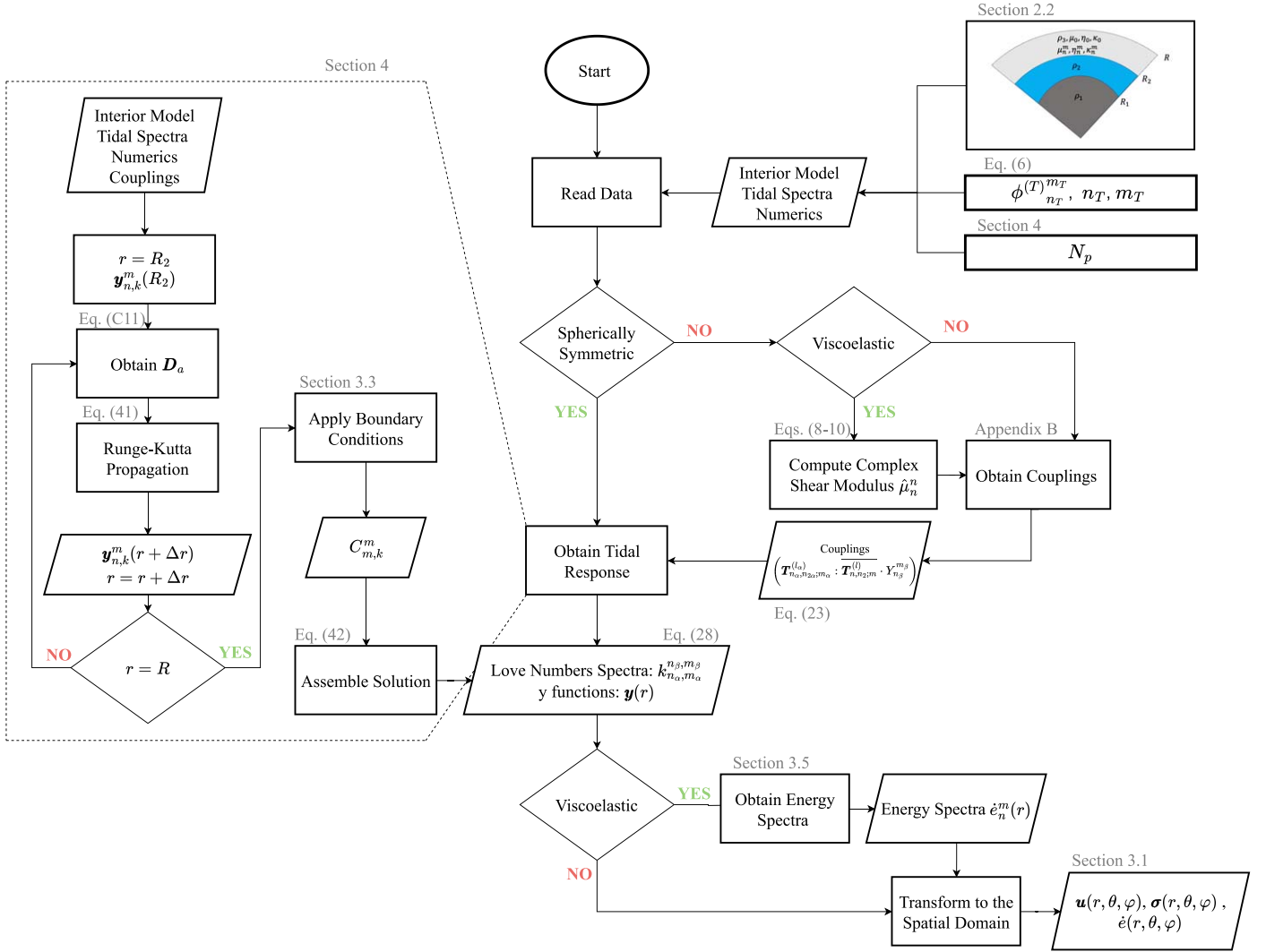
Section 2.2

$\rho_3, \mu_3, \eta_3, \kappa_3$
$\mu_n^m, \eta_n^m, \kappa_n^m$
ρ_2
ρ_1
R
R_2
R_1

Eq. (6)

$\phi^{(T)}{}_{n_T}^{m_T}, \; n_T, m_T$

Section 4

N_p

Start

Section 4

Interior Model
Tidal Spectra
Numerics
Couplings

$r = R_2$
$\boldsymbol{y}_{n,k}^m(R_2)$

Eq. (C11)

Obtain $\boldsymbol{D}_a$

Eq. (41)

Runge-Kutta
Propagation

$\boldsymbol{y}_{n,k}^m(r + \Delta r)$
$r = r + \Delta r$

NO $r = R$ YES

Section 3.3

Apply Boundary
Conditions

$C_{m,k}^m$

Eq. (42)

Assemble Solution

Read Data

Interior Model
Tidal Spectra
Numerics

Spherically
Symmetric   NO →   Viscoelastic   NO →

YES

Eqs. (8-10)   YES

Compute Complex
Shear Modulus $\hat{\mu}_n^n$

Appendix B

Obtain Couplings

Obtain Tidal
Response

Couplings
$\left(\boldsymbol{T}_{n_\alpha, n_{2\alpha}; m_\alpha}^{(l_\alpha)} : \overline{\boldsymbol{T}_{n, n_2; m}^{(l)}} \cdot Y_{n_\beta}^{m_\beta} \right)$

Eq. (23)

Eq. (28)

Love Numbers Spectra: $k_{n_\alpha, m_\alpha}^{n_\beta, m_\beta}$
y functions: $\boldsymbol{y}(r)$

Viscoelastic   YES →

Section 3.5

Obtain Energy
Spectra

Energy Spectra $\dot{e}_n^m(r)$

NO

Transform to the
Spatial Domain

Section 3.1

$\boldsymbol{u}(r, \theta, \varphi), \boldsymbol{\sigma}(r, \theta, \varphi),$
$\dot{e}(r, \theta, \varphi)$

Figure 1. Flowchart of the methodology employed to obtain the tidal response.

The spectral-perturbation method of Qin et al. (2014, 2016) provides an approximated solution whose accuracy is expected to decrease as the amplitude of lateral variations increases. To test the accuracy of the perturbation method, we consider an elastic Io-like body (Table 1, $\tau \to \infty$) with zonal—$(n_{LV}, m_{LV}) = (1, \; 0)$, $(n_{LV}, \; m_{LV}) = (2, \; 0)$—and sectoral—$(n_{LV}, m_{LV}) = (1, \; \pm 1)$—lateral variations under a zonal tidal forcing—$(n_T, m_T) = (2, \; 0)$—and compute the tidal response. We note that similar results are obtained for different interior parameters and forcing. For each of the considered lateral heterogeneities, we obtain the gravitational Love numbers using the two methods and compute the difference between them. The tidal response can be written as the tidal response of a spherically symmetric body, given by k_2^u, plus an additional response arising from lateral variations $\Delta k_{2,0}^{n,m}$.

Figure 2 shows the tidal Love number spectra for the three sets of lateral heterogeneities; first-, second-, and third-order modes are indicated. The additional tidal response increases from being 0.01% of the tidal response of the uniform body for peak-to-peak shear modulus variations of $\sim 0.1\%$ of the mean shear modulus to about 10% for variations of the same order of magnitude as the mean shear modulus. The additional tidal response is clearly dominated by first-order modes, which for small lateral variations are orders of magnitude higher than

second-order modes. However, the difference between first- and second-order modes decreases as the amplitude of lateral variations increases.

The results obtained with the spectral and the spectral-perturbation method show good agreement. Differences between the results obtained with the two models are as small as $\sim 10^{-5}\%$ for lateral variations of less than $\sim 10^{-3}\%$. The difference is likely caused by differences in how the equations are radially integrated; for instance, the difference decreases as the number of radial points used in the Runge–Kutta integration increases. This difference increases as the amplitude of lateral heterogeneities increases. However, it remains small even when substantial lateral heterogeneities are considered. For 10% peak-to-peak variations of the shear modulus, the difference remains below 1%; discrepancies of 10% or more are only attained when peak-to-peak variations of the shear modulus have the same order of magnitude as the mean shear modulus. The remarkable agreement is due to the fast decrease of mode amplitude with increasing mode order, as shown in Figure 2. This means that the effect of modes of higher-order modes on modes of lower order remains small even with high-amplitude lateral heterogeneities.

We also consider the case of an icy moon. We obtain the tidal response for the reference Enceladus model (Table 1) for various
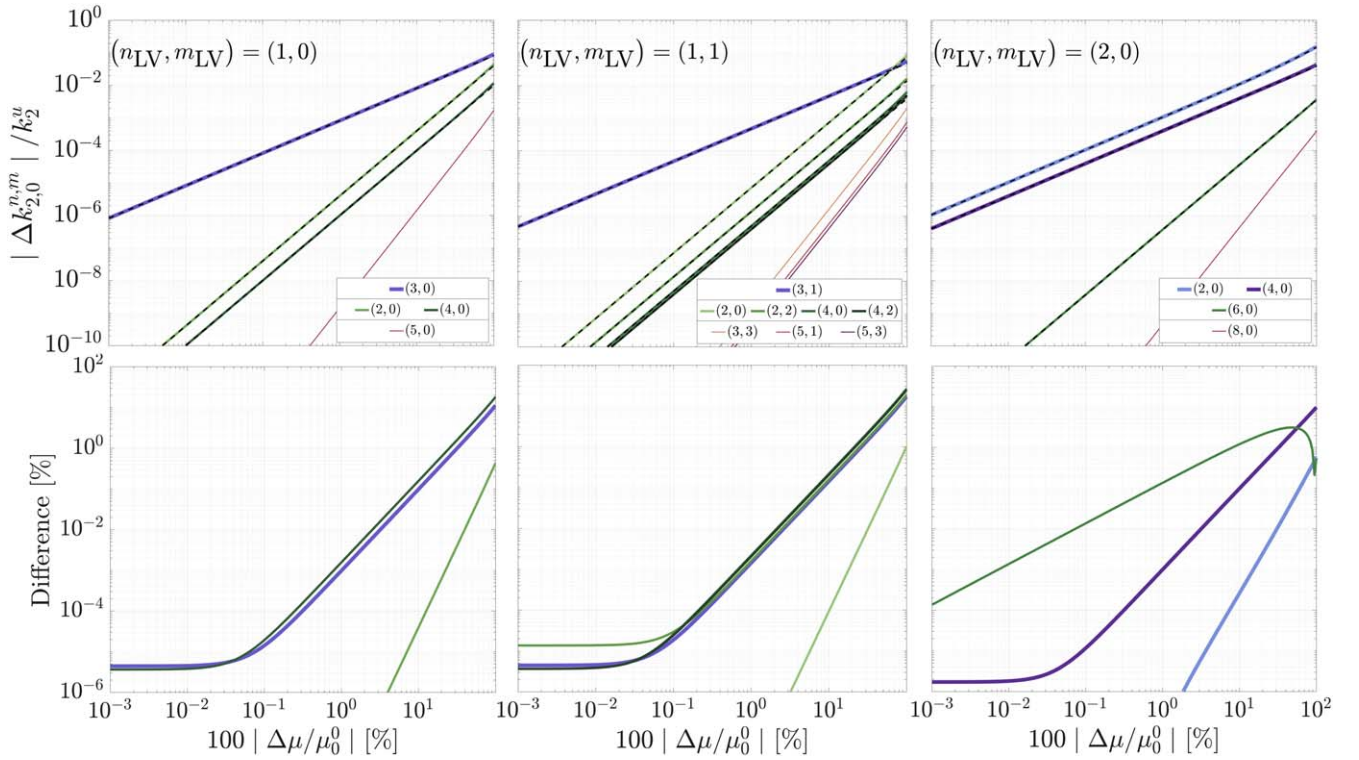
Figure 2. Gravitational Love numbers for different types of lateral shear modulus variations (upper panels), and the differences with the Love numbers obtained via the perturbation approach of Qin et al. (2014) (lower panels). An elastic Io (Table 1) with shear modulus variations of different wavelengths (n_{LV}, m_{LV}) is assumed. The amplitude of lateral variations is given in terms of the peak-to-peak variation of the shear modulus with respect to its mean. The solution is cut off at perturbation order 3. The line width indicates the order of the mode, with thicker lines indicating lower-order modes. In the upper panels, the dashed lines correspond to the solution obtained with the perturbation method of Qin et al. (2014). For (n_{LV}, m_{LV}) = (1, 1), only the $+|m|$ modes are shown, but $-|m|$ modes of amplitude $k_{2,0}^{n,-|m|} = (-1)^{|m|} k_{2,0}^{n,|m|}$ are also excited. The difference between the two methods is computed as $100|(k_{2,0}^{n,m}/k_2^u)_R - (k_{2,0}^{n,m}/k_2^u)_Q|/|k_{2,0}^{n,m}/k_2^u|_R$, with R and Q standing for the method presented here and the method of Qin et al. (2014), respectively.

types of lateral variations using both spectral methods and the FEM code. For the FEM approach, we adapt the methodology outlined in Berne et al. (2023a) and Berne et al. (2023b) to develop an FEM capable of simulating tidal deformation on laterally heterogeneous ocean worlds. FEMs solve the equation of motion for quasi-static problems by formulating 3D displacements (i.e., in response to applied forces and boundary conditions) as a series of linear shape functions across a mesh domain. For this work, we discretize mesh domains using tetrahedra with a maximum edge length of 1 km and consider between $18 \cdot 10^6$ and $33 \cdot 10^6$ elements for each simulation. To simulate tidal loading, we upload mesh geometries to a modified version of the geodynamic software package Pylith (Aagaard et al. 2007), which can self-consistently consider forces arising from external tidal potentials, self-gravity, and radial displacements at boundaries between internal density layers (for additional details, see Supplementary S1.1 of Berne et al. 2023a). To incorporate lateral variations in elastic properties, we sample analytic basis functions (i.e., spherical harmonics) for a given heterogeneity at mesh node locations. Following simulations, we expand displacements into spherical harmonics and compute Love numbers for comparison to semi-analytic solutions presented in this work.

Figure 3 compares the results obtained with the three methods (i.e., spectral method, spectral-perturbation method, and FEM). With few exceptions, the results obtained with the FEM and the spectral method show the best agreement. As explained above, the difference between the spectral and spectral-perturbation method grows with the amplitude of lateral variations reaching values as high as 5% for peak-to-

peak shear modulus variations of 50%. In contrast, the difference between results obtained with the spectral and the FEM remains below 1% and is often 1 order of magnitude smaller than for the former. We ascribe small discrepancies between results with the spectral method and the FEM code to errors associated with resolution. We find that the agreement between both methods improves when the FEM mesh size decreases from 5 to 1 km.

To benchmark the viscoelastic component, we compute the Love numbers of a spherically symmetric uniform body obtained using analytical expressions (e.g., Matsuyama et al. 2018) and *LOV3D*, and we find excellent agreement (relative differences of $<10^{-6}$%). For a viscoelastic body with lateral variations, we check that energy dissipation is computed self-consistently by comparing the total energy dissipation obtained using the two approaches outlined in Section 3.5 (i.e., Equations (34) and (37)), finding good agreement (see Appendix E).

6. The Tides of a Laterally Heterogeneous Elastic Body

Figure 2 evidences that different spatial patterns of lateral variations result in distinct tidal responses. This is further illustrated in Figure 4, which shows the degree 2 gravitational Love spectra for *monochromatic* (single total and zonal wavenumber) shear modulus variations. Each type of lateral variations leads to a unique Love number spectra. Hence, if the full tidal response were measured, the inverse problem could be solved and the spatial pattern and amplitude of lateral variations inferred; this technique is known as *tidal tomography*.
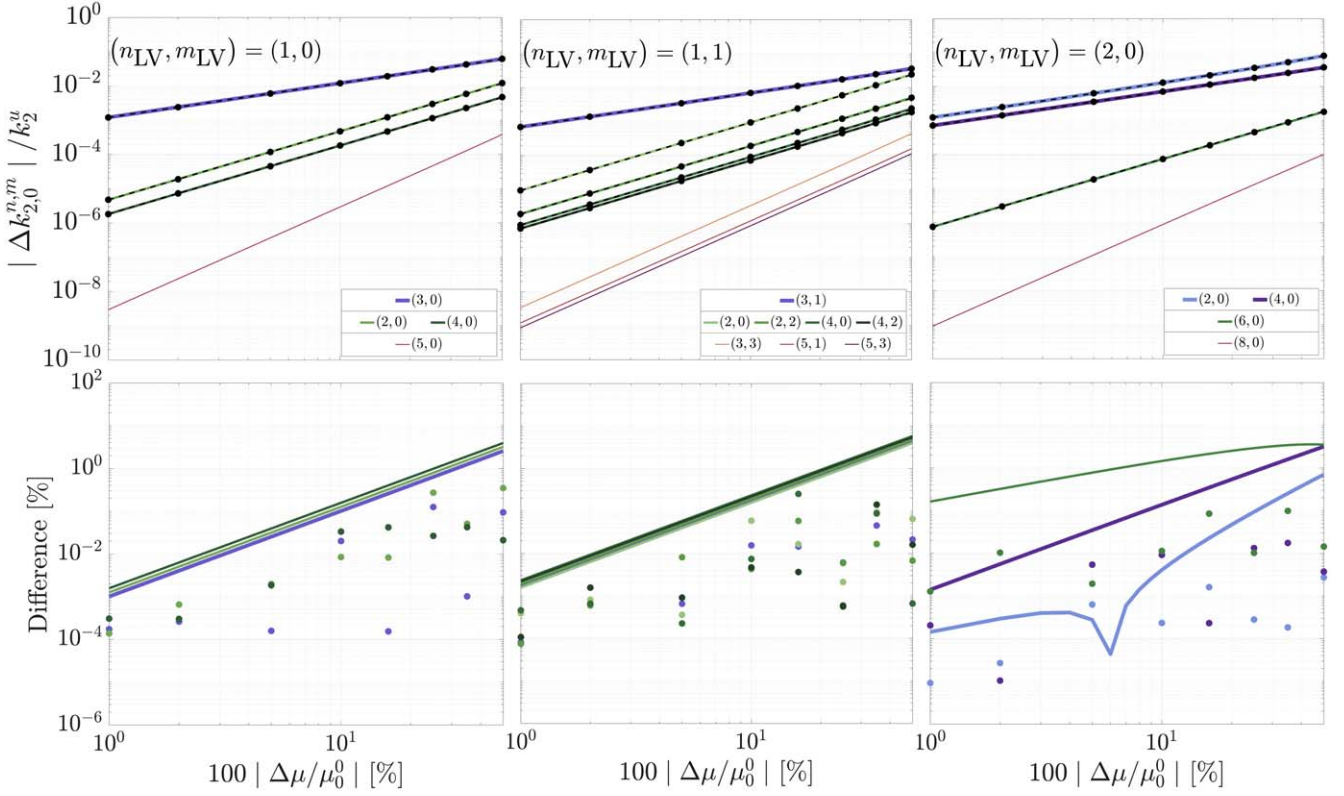
Figure 3. Same as Figure 2, but for the Enceladus model (Table 1). Differences are obtained as $100|(\Delta k_{2,0}^{n,m}/k_2^u)_R - (\Delta k_{2,0}^{n,m}/k_2^u)_X|/|\Delta k_{2,0}^{n,m}/k_2^u|_R$, where X can either be the results obtained using the FEM model or the spectral-perturbation method. Solutions obtained using the FEM of Berne et al. (2023a) and the perturbation method of Qin et al. (2014) are indicated with filled circles and dashed lines, respectively.
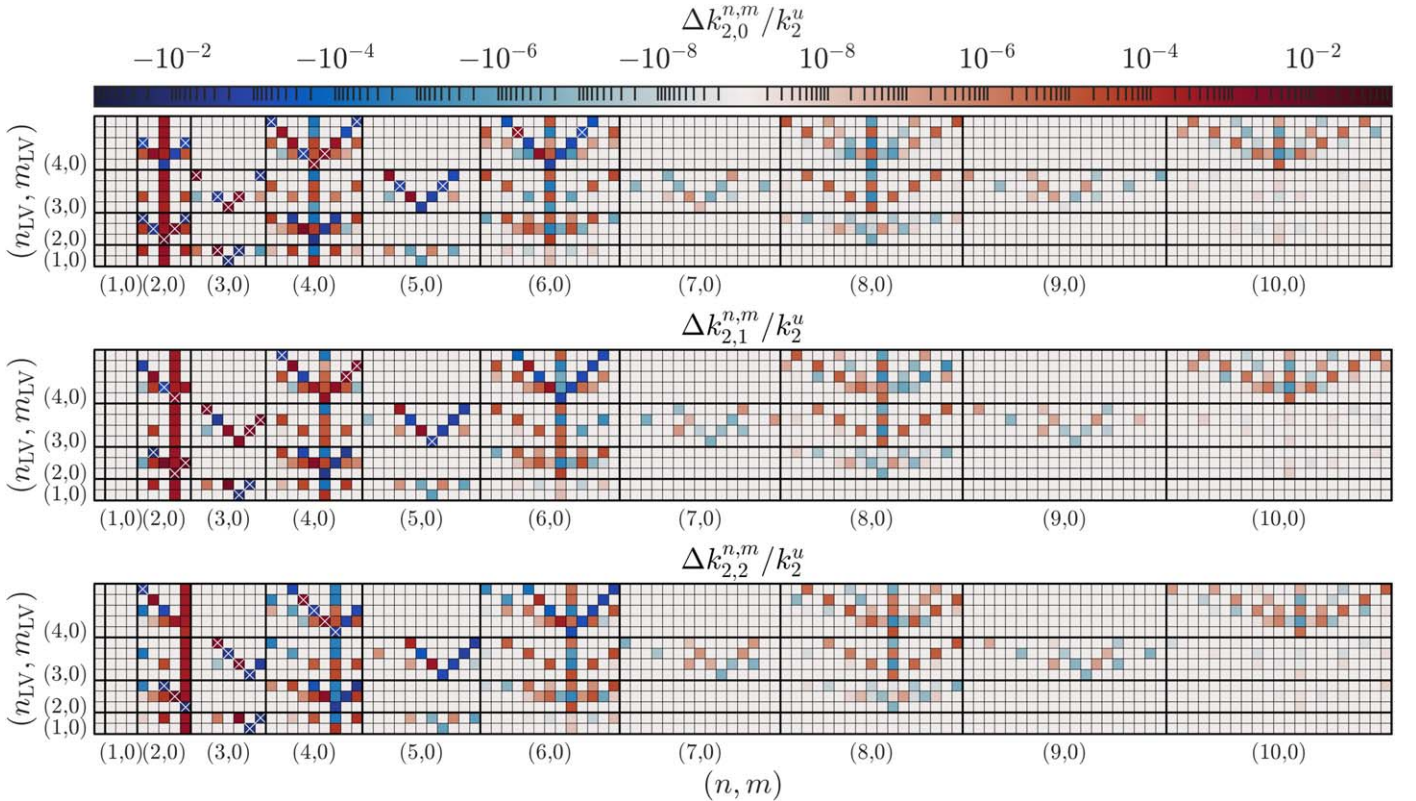

Figure 4. Love number spectra for degree 2 and orders 0 (upper panel), 1 (center panel), and 2 (lower panel) tidal forcings for lateral variations of different degrees and orders (n_{LV}, m_{LV}). An elastic Io is assumed (Table 1), and the solution is cut off at perturbation order 4. Color intensity indicates the strength of the mode, and the terms with highest amplitude are indicated with a cross. For all cases, we assume peak-to-peak shear modulus variations of 10% of the mean shear modulus.
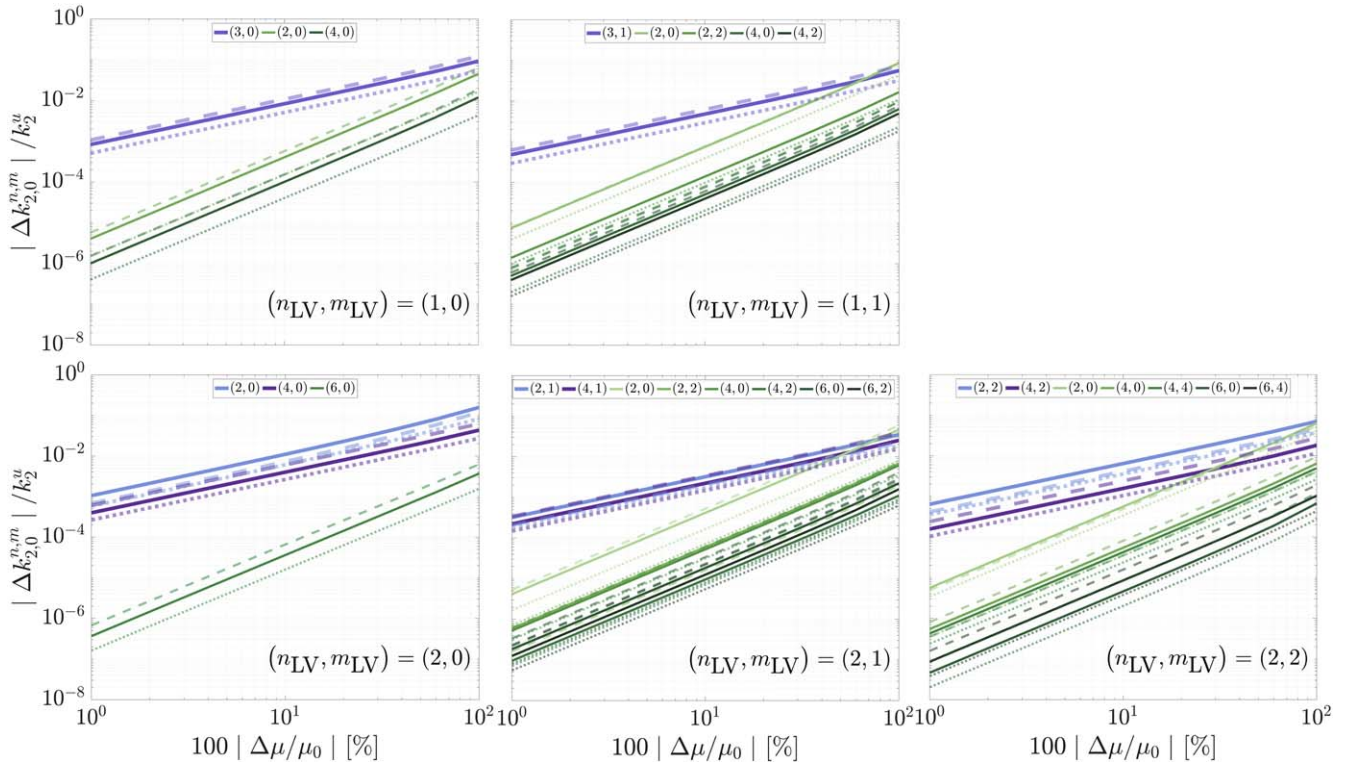
Figure 5. Gravitational Love numbers, $k_{2,0}^{n,m}$, for lateral shear modulus variations of different wavelengths (n_{LV}, m_{LV}) for Io (solid lines), the Moon (dashed lines), and Mercury (dotted lines).

The use of tidal tomography presents several challenges. The amplitude of the additional tidal response arising from lateral variations is small, making it challenging to measure. Because of this, we can expect that only the terms with the highest amplitudes will be measured. Moreover, lateral variations in different regions and of different properties (e.g., elastic properties and layer thickness) can result in a similar tidal spectra. Finally, lateral variations are likely not monochromatic but feature various wavelengths. This makes the solution of the inverse problem nonunique. As an example, both degree 1 and degree 3 lateral variations produce a degree 3 tidal signal (see Figure 4). If no other terms of the spectra are measured, a degree 3 response would be indicative of a hemispherical dichotomy but could not be used to distinguish between degree 3 and degree 1 lateral variations. Distinguishing between the two would require measuring the degree 5 tidal response, which is more prominent for degree 3 lateral variations. Lateral variations also alter the tidal response at the degree and order of the forcing, most prominently for degree 2 variations. This makes it challenging to distinguish the effects of lateral heterogeneity from the tidal response, and it might even result in errors when estimating the mean properties of the body. In such cases, a way to detect lateral variations is by comparing the k_2 Love numbers at different orders, which are only equal if the body is spherically symmetric. The tidal potential of a moon in an eccentric orbit has both order 0 and order 2 components, making this approach attractive.

So far, tidal tomography has just been used for Earth (Lau et al. 2017), for which there is high-quality geodetic data. However, future space missions might make it possible to use tidal tomography for other Solar System bodies. Figure 5 shows the gravitational Love number spectra for Io, the Moon, and Mercury (Table 1). In all cases, the additional tidal

response (Δk) is normalized by the tidal response of the spherically symmetric body (k_2^u), listed in Table 1.

The Gravity Recovery and Interior Laboratory (GRAIL) mission provided very accurate lunar gravity data, which can be used to constrain the amplitude of lateral heterogeneities in the Lunar interior (Qin et al. 2014). We caution that a comprehensive inversion can only be done if an expression for the Love numbers that account for the effect of lateral variations (i.e., Equation (28)) rather than the classic expression often used (e.g., Konopliv et al. 2013), is used when obtaining the gravity solution from raw GRAIL data, and the model parameter space is thoroughly sampled. However, the results shown in Figure 5, combined with the available GRAIL gravity field, give a qualitative impression of the amplitude of lateral variations. For instance, Williams et al. (2014) showed that the measured degree 3 response of the Moon is consistent with a spherically symmetric model; this suggests that there are not high-amplitude odd-degree lateral variations, as otherwise one would measure a high degree 3 response. Additionally, the degree 2 orders 0 and 2 Love numbers of the Moon differ by ~1%, but are within the uncertainty of the measurements (Konopliv et al. 2013; Lemoine et al. 2013). From Figure 5, this suggests that degree 2 variations are less than ~10%.

Of the three bodies, Mercury is the one for which the additional tidal response is the smallest relative to the tidal response of a spherically symmetric. Nevertheless, as Mercury is the body with the highest k_2^u, lateral variations lead to the highest gravity signal in absolute terms. The *MESSENGER* mission measured Mercury's k_2 with an accuracy of approximately 5%, insufficient to observe lateral variations. In contrast, BepiColombo, scheduled to start its science operations in 2026, is expected to improve the accuracy to ~0.1% (Genova et al. 2021). The accuracy at which the nondiagonal
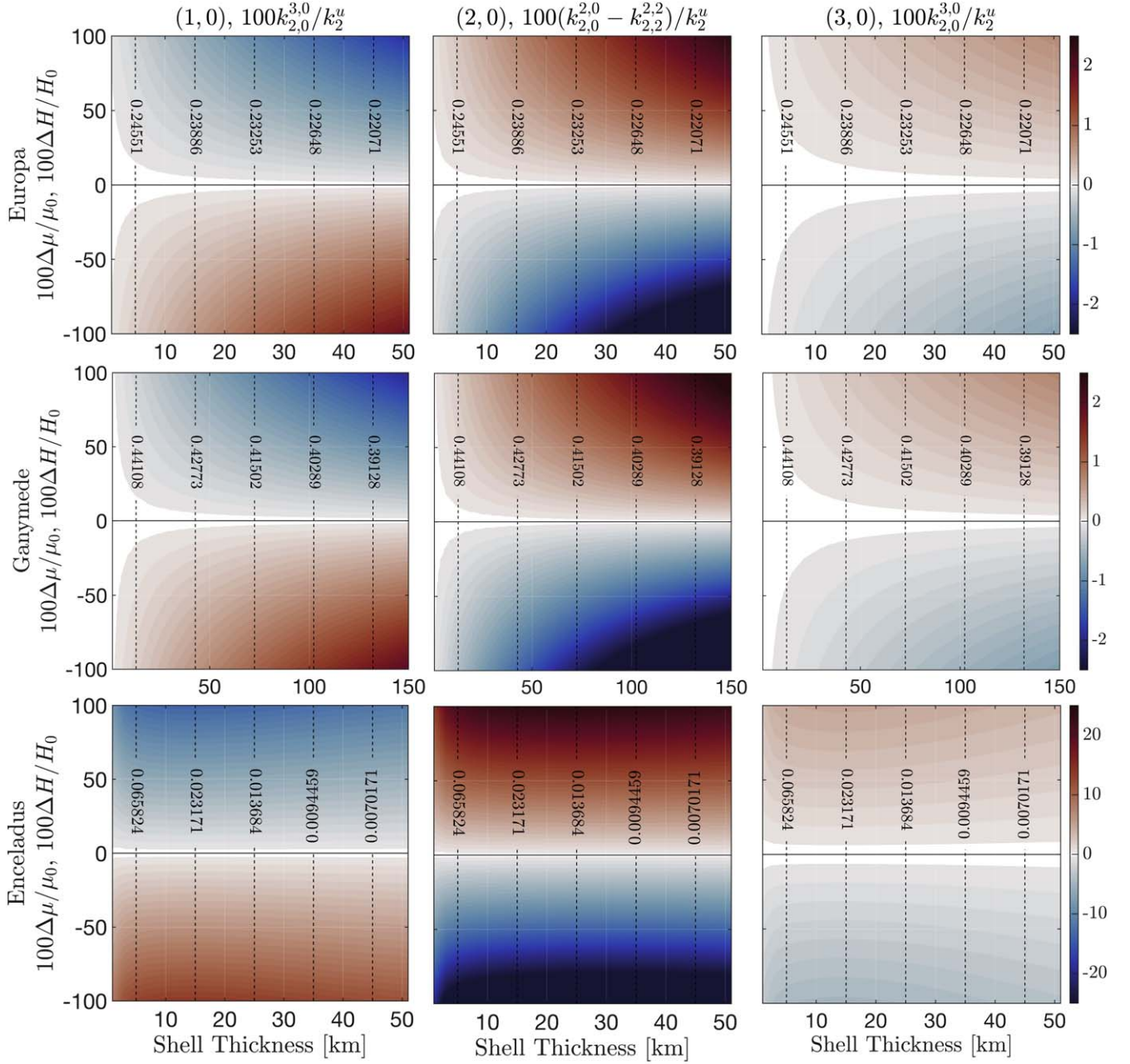
Figure 6. Effect of lateral heterogeneities of different wavelengths for Europa (first row), Ganymede (second row), and Enceladus (third row). The highest-amplitude components of the tidal responses arising from zonal lateral variations of degrees 1 (first column), 2 (second column), and 3 (third column) are depicted. For reference, the degree 2 Love number of a spherically symmetric body, k_2^u, is indicated (dashed black lines).

Love numbers can be obtained (e.g., $k_{n_\alpha, m_\alpha}^{n_\beta, m_\beta}$, with $n_\alpha \neq n_\beta$, $m_\alpha \neq m_\beta$) can only be determined via a simulation of BepiColombo's gravity science experiment. Assuming the accuracy inferred for k_2 extends to the other Love numbers, variations of the shear modulus or of the thickness of Mercury's rocky envelope as small as 2% might be detected. As demonstrated by Figure 5, the detection threshold depends on the spatial pattern of lateral variations.

We also consider the role of lateral heterogeneities in icy moons. As noted in Section 2.2, shell-thickness variations can be approximately mapped to shear modulus variations, provided the shell is thin compared to the moon's radius. This is the case for icy moons—for Europa and Ganymede, the shell to radius ratios are ∼0.02 and 0.05, respectively; for Enceladus,

the ratio is higher, at ∼0.1, making the approximation less accurate. Figure 6 shows the additional tidal response for zonal variations of the shear modulus for Europa, Ganymede, and Enceladus. The relative additional tidal response resulting from lateral variations ($\Delta k_{n_T, m_T}^{n, m}/k_{n_T}^u$) is approximately 1 order of magnitude higher for Enceladus than for the two Jovian moons. For Enceladus, lateral variations of 50% cause an additional tidal response ∼10% the amplitude of the main tidal response (see also Berne et al. 2023a and Běhounková et al. 2017), while for the latter the additional tidal response is ∼1%. Nevertheless, as k_2 of Enceladus is more than 1 order of magnitude smaller (Table 1), $\Delta k_{n_T, m_T}^{n, m}$ is similar for the three icy moons.

The possibility to observe lateral variations depends on their amplitude and the accuracy to which the Love number spectra
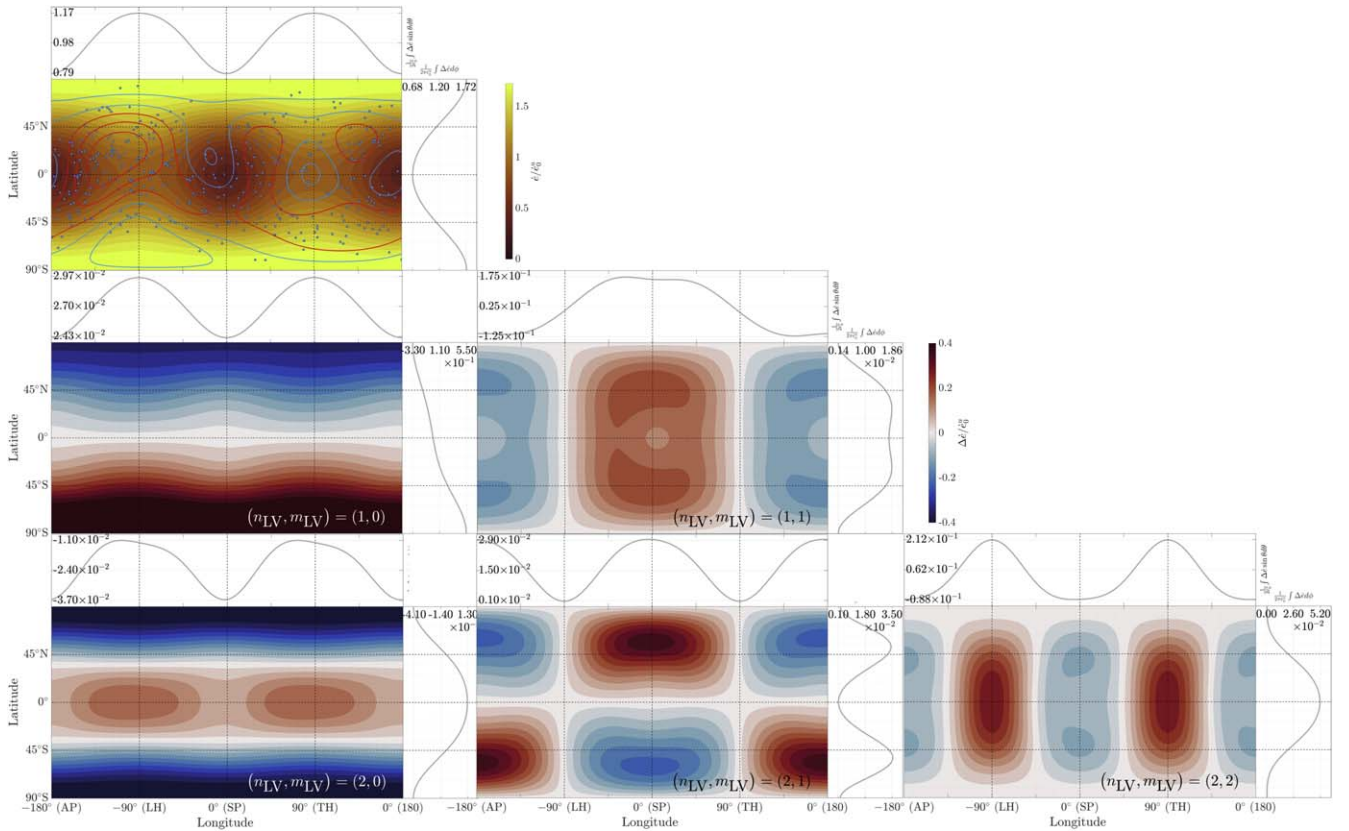
Figure 7. Pattern of tidal heating for a spherically symmetric body (upper row) and for bodies with different types of lateral viscosity variations. For the spherically symmetric body, the total heating pattern is shown; for the rest, the difference between their corresponding heating pattern and that of a spherically symmetric body is shown. All plots are normalized by the average tidal heating of the spherically symmetric body. The reference Io model is employed (see Table 1) with peak-to-peak viscosity variations of 50%. The subplanet (SP) and antiplanet (AP) points as well as the centers of the trailing and leading hemispheres (TH and LH) are indicated. The longitudinally and longitudinally averaged tidal heating are also shown. In the first panel, Io's volcanoes are indicated (blue dots), with contours corresponding to the density of Io's volcanoes (red and blue contours indicating values higher and lower than the global average) (Steinke et al. 2020).

can be obtained. For Enceladus, gravity and shape data indicate that shell-thickness varies from 29 km at the equator to 7 km at the south pole (Čadek et al. 2016; Beuthe et al. 2016; Hemingway & Mittal 2019). In contrast, shell-thickness variations for Europa are not expected to exceed 7 km (Nimmo et al. 2007). Ganymede's shell-thickness variations are not constrained, yet ocean circulation models predict shell-thickness variations to be smaller for big icy moons (Kang & Jansen 2022). This makes Enceladus a prime candidate for the use of tidal tomography in the future. With the JUpiter Icy Moons Explorer (JUICE) on its way to the Jovian system, it is interesting to consider if it can pick up the signal arising from lateral variations of shell properties. JUICE will measure Ganymede's k_2 with an expected accuracy of 10^{-4} (Cappuccio et al. 2020), which is less than 0.1% of Ganymede's expected k_2. This accuracy is sufficient to detect differences in $k_{2,0}^{2,0}$ and $k_{2,2}^{2,2}$ caused by lateral variations of ice shell properties, making tidal tomography a promising tool for constraining lateral variations in Ganymede's shell.

7. The Tides of a Laterally Heterogeneous Maxwell Body

In the previous section, we considered the tidal response of an elastic body with lateral variations. We will now consider how lateral variations affect the tidal response of a viscoelastic body. If a body is not perfectly elastic, part of the tidal energy is converted into heat. Here, we explore the effect that lateral variations of the viscosity has on tidal heating patterns.

We employ our reference Io model (see Table 1) and consider various patterns of viscosity variations. The complex shear modulus spectra is obtained using Equations (8)–(10). Even in the case of monochromatic viscosity variations, the complex shear modulus spectra is not monochromatic but contains infinite terms of varying amplitude. To use the spectral method, the complex shear modulus spectra needs to be cut off. We consider terms up to 2 orders of magnitude smaller than the leading non-degree-0 term of the complex shear modulus. The heating pattern depends on the tidal potential spectra. We focus on the tides experienced by a synchronous body in an eccentric orbit with zero obliquity—for which we give the tidal potential in Appendix D. We obtain the tidal response for each component of the tidal potential and compute the energy spectra as described in Section 3.5.

Figures 7 and 8 show the spatial distribution of tidal heating for various types of monochromatic lateral viscosity variations and the corresponding spectra (Equation (31)), respectively. Even for a spherically symmetric body, tidal heating is not homogenously distributed within the interior. For the considered tidal forcing, the heating pattern consists of terms of degree and order (0, 0), (2, 0), (2, ± 2), (4, 0), (4, ± 2), and (4, ± 4) (e.g., Beuthe 2013). For the three-layer model considered here (solid core, liquid core, and rocky envelope), tidal heating is maximum at the poles; along the equator, tidal heating exhibits minima at the subplanet (0°) and antiplanet (180°) points and maxima at the center of the trailing and leading hemispheres (90° and −90°, respectively). Viscosity
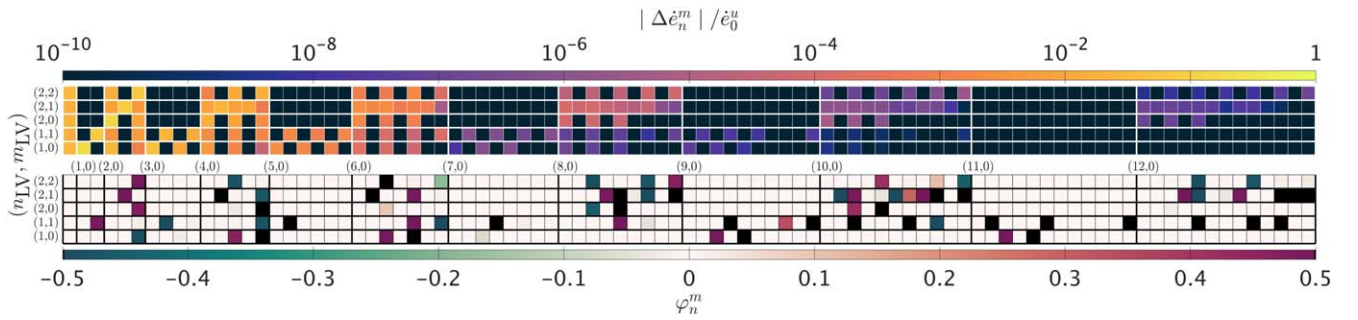
Figure 8. Tidal heating spectra (Equation (31)) corresponding to the cases of Figure 7. The energy spectra is given in terms of amplitude (upper panel) and the longitudinal eastward shift in the fraction of longitudinal wavelength with respect to $\Re(Y_n^m)$ (lower panel).

lateral variations introduce additional terms. The difference between the tidal heating pattern of a uniform body and a body with lateral variations is dominated by the same pattern as the considered viscosity variations. For example, a polar dichotomy of degree 1 and order 0 in viscosity translates into the same dichotomy in tidal heating (see second panel in Figure 7). This also follows from the tidal heating spectra, where the most prominent terms are those with same wavelength as the considered viscosity variations (Figure 8). Apart from this dominant term, other terms with smaller amplitude also arise.

Some terms of the tidal heating spectra are not symmetric with respect to the 0° meridian. This is most evident when looking at the tidal heating map corresponding to the lateral variations of degree 2 and order 0, where we observe a westward shift in the longitude at which the minimum heat flux is attained compared to the spherically symmetric case. The appearance of a trailing–leading hemisphere asymmetry is remarkable since the considered patterns of lateral variations do not contain such an asymmetry. A similar phenomenon was observed by Steinke et al. (2021), who used FEM to obtain tidal heating patterns for a multilayered, laterally heterogeneous Io. The asymmetry arises because the tidal potential is not symmetric with respect to the east–west direction. As shown in Appendix D, the tidal potential can be broken into a degree 2 and order 0 standing wave, and degree 2 and order 2 westward and eastward-propagating waves of different amplitudes. The amplitude of the eastward component is greater than that of the westward component, breaking the symmetry of the problem. No asymmetry is observed if a single standing wave is considered.

Tidal heating patterns can help constrain the interior properties of rocky and icy worlds (e.g., Breuer et al. 2022). The distribution of volcanoes in Io has been used as a proxy of tidal heating. In Io, the concentration of volcanoes is greater toward middle to low latitudes, and it is bimodal, exhibiting two maxima 30°–60° eastward of the sub-Jovian and anti-Jovian points (see Figure 7). Moreover, the distribution of volcanoes also contains a statistically significant degree 6 component (Kirchoff et al. 2011; Hamilton et al. 2013; Steinke et al. 2020). The link between tidal heating and volcanic patterns is not simple: convection and melt transport affect how the two patterns relate (Steinke et al. 2020a), and the inferred volcanic patterns are affected by biases in observations. Recent observations by the Juno spacecraft have discovered new volcanoes in previously poorly covered polar regions and even hinted that the north pole could have a higher concentration of hot spots (Zambon et al. 2023; Davies et al. 2024).

The tidal heating pattern characteristic of a three-layer (solid core, liquid core and rocky envelope) spherically symmetric Io

does not match the observed distribution of volcanoes. As illustrated in Figure 7, the surface heat flux peaks at the poles, does not exhibit a 30°–60° eastward shift with respect to the tidal axis, and does not have degree 6 terms nor a polar dichotomy. The heating pattern is affected by both radial and lateral variations of internal properties. The presence of a low-viscosity asthenosphere can account for the concentration of volcanoes at middle to low latitudes. However, spherically symmetric models cannot reproduce the observed eastward shift of volcanic activity with respect to the sub-Jovian point. Tyler et al. (2015) showed that tidal heating in a magma ocean can cause this shift. The results discussed here, as well as the FEM model of Steinke et al. (2021), indicate that lateral viscosity variations can introduce a longitudinal shift. The magnitude and direction of the longitudinal shift depend on the particular form of lateral and radial variations of internal properties. A comprehensive exploration of the joint effect of radial and lateral variations is left for future work. As evidenced in Figure 8, lateral variations of internal properties can also introduce a degree 6 heat flux pattern and cause a polar dichotomy (terms with odd m).

Interior properties and heating patterns are tightly related. Viscosity and shear modulus depend on temperature and melt fraction. Lateral variations of tidal heating affect both quantities (Steinke et al. 2020a) and hence the heating pattern. This feedback can have important implications for the interior evolution of tidally active bodies. As shown in Figure 8, even a body with a uniform interior exhibits nonuniform tidal heating. Such a pattern will alter material properties and feedback into the heating pattern, driving interior evolution. Alternatively, primordial lateral heterogeneities might be amplified by the feedback in a similar way. The extent to which this happens depends on how heat is transported within the body. Tackling this complex problem requires coupling a tidal and a thermal model. The lower computational cost of spectral methods compared to FEM methods makes them an attractive tool to approach the problem.

8. Summary and Outlook

In this work, we presented a spectral method to compute the tidal response of bodies with lateral heterogeneities, and we applied it to elastic and viscoelastic bodies. Below, we summarize the key points:

1. The new spectral method shows good agreement with results obtained with the spectral-perturbation approach of Qin et al. (2014) and the FEM model of Berne et al. (2023a, 2023b). Differences between the results obtained with the new method and the perturbation method grow

as the amplitude of lateral variations increases. Predictions obtained using the perturbation method differ by less than 1% for shear modulus variations of $\lesssim$10% and only reach $\sim$10% for peak-to-peak variations of the same order of magnitude as the mean shear modulus. This makes the perturbation method a powerful tool to compute the tidal response of bodies, unless such variations have high amplitude. Differences between the FEM approach and the presented spectral method remain small even for high-amplitude lateral variations. Spectral methods are more computationally efficient: a model that takes $\sim$10 days to run using the FEM code in a two-core computer is solved in less than a minute using the spectral method presented here; in terms of memory, the grids employed in the FEM runs presented here required $\sim$1 GB of memory, while the coupling matrices employed in the spectral model required $\sim$1 MB. This makes spectral methods more suitable to tackle the inverse problem. However, unlike FEMs, the spectral code presented here cannot include faults, cracks, or nonlinear rheology, and layer thickness variations can only be treated by mapping them to shear modulus variations (Berne et al. 2023a).

2. Each set of lateral variations results in distinct Love number spectra. Thus, measurements of the complete tidal response of a body can be used to constrain lateral variations. Nevertheless, the solution of the inverse problem is nonunique, as it is unlikely that the complete Love number spectra can be measured and lateral variations at different depths might result in similar spectra (Section 6). Other measurements, such as static gravity and topography, might help to solve this degeneracy.

3. For the Moon, Io, and Mercury, shear modulus variations of the same order of magnitude as the mean shear modulus can cause an additional tidal response as high as $\sim$1%–10% of the main tidal response. BepiColombo should observe the fingerprint of lateral variations, provided they are higher than approximately 2% of the mean shear modulus (Section 6).

4. In icy worlds, lateral variations of ice shell thickness modify the tidal response. Due to the expected amplitude of shell-thickness variations, Enceladus is a prime candidate to use tidal tomography. For Europa and Ganymede, shell-thickness variations can lead to an additional tidal response on the order of 0.1%–1% of the main tidal response depending on their amplitude. The accuracy of JUICE makes it possible to detect this signal (Section 6).

5. Lateral variations modify the distribution of tidal heating for viscoelastic bodies. The additional tidal heating pattern due to lateral variations of the viscosity is dominated by the pattern of such variations. Lateral viscosity variations can cause a trailing–leading hemisphere asymmetry in tidal heating. This could explain the eastward shift of volcanic activity with respect to the sub-Jovian and anti-Jovian points observed in Io (Section 7).

6. The dependence of interior properties on temperature and melt fraction, which in turn depend on the distribution of tidal heating, gives rise to a complex feedback that can drive interior evolution. The computational efficiency of the spectral method makes it a good candidate to study this feedback (Section 7).

7. For this work, we considered a simplified interior structure consisting of a solid nondeformable core, overlaid by a hydrostatic liquid and a solid envelope with radially uniform properties (Section 2.2). These assumptions can be relaxed—i.e., the deformation of the inner core can be considered, dynamic liquid tides included, and radial variations of interior properties introduced.

Appendix A
Tensor Spherical Harmonics

Tensor spherical harmonics are a generalization of spherical harmonics to tensors of rank >0. For problems with spherical geometry, expanding the tensors in tensor spherical harmonics allows to employ the properties of tensor spherical harmonics to eliminate longitude and latitude from the equations of motion. A rank k tensor $\boldsymbol{a}$ can be written as (James & Cook 1976)

$$\boldsymbol{a} = \sum_{n,m,\ n_1,..,n_k} a^m_{n,n_1,..n_k} \boldsymbol{Y}^m_{n,n_1,..n_k}. \quad (A1)$$

Below, we define tensor spherical harmonics and introduce some of their main properties. We also give explicit expressions of tensor spherical harmonics of ranks 0, 1, and 2; explain how to transform between them and other bases often used in literature and in this manuscript; and list operators used in the text. An exhaustive list of properties can be found in James & Cook (1976).

A.1. Definitions

Tensor spherical harmonics of degree n and order m of rank k are recursively defined as (James & Cook 1976)

$$\boldsymbol{Y}^m_{n,n_1..n_k} = (-1)^{n-m}\Lambda(n)\sum_{m_1,\mu}\begin{pmatrix} n & n_1 & 1 \\ m & -m_1 & -\mu \end{pmatrix}\boldsymbol{Y}^{m_1}_{n_1,..n_k}\boldsymbol{e}_\mu, \quad (A2)$$

with the 2×3 array being the Wigner 3-j coefficient, and $\Lambda(a, b, c..)$ is given by

$$\Lambda(a, b, c,...) = ((2a + 1)(2b + 1)(2c + 1)...)^{1/2}. \quad (A3)$$

$\boldsymbol{e}_\mu$ are defined in terms of the unit vectors of Cartesian coordinates $(\mathbf{1}_x, \mathbf{1}_y, \mathbf{1}_z)$ as

$$\boldsymbol{e}_0 = \mathbf{1}_z \quad \boldsymbol{e}_{-1} = (\mathbf{1}_x - \mathrm{i}\mathbf{1}_y)\big/\sqrt{2} \quad \boldsymbol{e}_1 = -(\mathbf{1}_x + \mathrm{i}\mathbf{1}_y)\big/\sqrt{2}. \quad (A4)$$

The Wigner 3-j symbols are only nonzero when n, $n_1..n_k$ satisfy the triangular identity, which means that a rank k tensor

spherical harmonic of degree and order n and m have 3^k tensor spherical harmonics.

For convenience, we will sometimes use $\boldsymbol{Y}_{n_\alpha(k)}$ to refer to $\boldsymbol{Y}_{n_\alpha,n_{1\alpha},...,n_{k\alpha}}^{m_\alpha}$

Tensor spherical harmonics form an orthogonal basis. Integrated over the unit sphere, we have that

$$\frac{1}{4\pi}\int_\Omega \boldsymbol{Y}_{n_\alpha(k)} \cdot \boldsymbol{Y}_{n_\beta(k)}^{*}\mathrm{d}\Omega = \delta_{n_\alpha(k)}^{n_\beta(k)}, \qquad (A5)$$

where * indicates the complex-conjugate transpose. $\delta_{n_\alpha(k)}^{n_\beta(k)}$ is defined as $\delta_{m_\alpha}^{m_\beta}\delta_{n_\alpha}^{n_\beta}\delta_{n_{1\alpha}}^{n_{1\beta}} \dots \delta_{n_{k\alpha}}^{n_{k\beta}}$, where δ_a^b is the Kronecker delta; and $\cdot$ is the generalized dot product of two tensors defined in James & Cook (1976) as

$$\boldsymbol{e}_{\mu_1} \dots \boldsymbol{e}_{\mu_k} \cdot \bar{\boldsymbol{e}}_{\lambda_k} \dots \bar{\boldsymbol{e}}_{\lambda_1} = \delta_{\mu_1}^{\lambda_1} \dots \delta_{\mu_k}^{\lambda_k}. \qquad (A6)$$

The complex conjugate of a tensor spherical harmonic of rank k is given by

$$\overline{\boldsymbol{Y}_{n(k)}^m} = (-1)^{n+n_k+m+k}\boldsymbol{Y}_{n(k)}^{-m}, \qquad (A7)$$

which implies that, if a tensor is real, the m and $-m$ components are related as

$$\overline{a_{n(k)}^m} = (-1)^{n+n_k+m+k}a_{n(k)}^{-m}. \qquad (A8)$$

A.2. Rank 0 Tensors

Rank 0 tensor spherical harmonics are the classic spherical harmonics Y_m^n

$$Y_n^m(\theta, \varphi) = \sqrt{\frac{(2n+1)(n-m)!}{(n+m)!}}\, P_n^m(\cos\theta)\mathrm{e}^{\mathrm{i}m\varphi}, \qquad (A9)$$

where P_n^m are associated Legendre functions:

$$P_n^m(x) = (-1)^{n+m}\frac{(1-x^2)^{m/2}}{2^n n!}\frac{\mathrm{d}^{m+n}(1-x^2)^n}{\mathrm{d}x^{m+n}}. \qquad (A10)$$

A.3. Rank 1 Tensors

Rank 1 tensors, such as the displacement vector $\boldsymbol{u}$, are expanded using tensor spherical harmonics of rank 1, which can be written in spherical coordinates as

$$\sqrt{n(2n+1)}\,\boldsymbol{Y}_{n,n-1}^m = nY\boldsymbol{e}_r + E\boldsymbol{e}_\theta + G\boldsymbol{e}_\varphi, \qquad (A11a)$$

$$\sqrt{n(n+1)}\,\boldsymbol{Y}_{n,n}^m = \mathrm{i}G\boldsymbol{e}_\theta - \mathrm{i}E\boldsymbol{e}_\varphi, \qquad (A11b)$$

$$\sqrt{(n+1)(2n+1)}\,\boldsymbol{Y}_{n,n+1}^m = -(n+1)Y\boldsymbol{e}_r + E\boldsymbol{e}_\theta + G\boldsymbol{e}_\varphi, \qquad (A11c)$$

with

$$Y = Y_n^m,\ E = \frac{\partial Y}{\partial\theta},\ F = \frac{\partial^2 Y}{\partial\theta^2},$$
$$G = \csc\theta\frac{\partial Y}{\partial\varphi},\ H = \frac{\partial G}{\partial\varphi}. \qquad (A12)$$

Rank 1 tensor spherical harmonics are related to the scaloidal-poloidal-toroidal basis $(\boldsymbol{R}_n^m, \boldsymbol{S}_n^m, \boldsymbol{T}_n^m)$ as

$$\boldsymbol{R}_n^m = Y\boldsymbol{e}_r = \sqrt{\frac{n}{2n+1}}\,\boldsymbol{Y}_{n,n-1}^m - \sqrt{\frac{n+1}{2n+1}}\,\boldsymbol{Y}_{n,n+1}^m \qquad (A13a)$$

$$\boldsymbol{S}_n^m = E\boldsymbol{e}_\theta + G\boldsymbol{e}_\varphi = \sqrt{\frac{n}{2n+1}}\,(n+1)\boldsymbol{Y}_{n,n-1}^m + \sqrt{\frac{n+1}{2n+1}}\,n\boldsymbol{Y}_{n,n+1}^m \qquad (A13b)$$

$$\boldsymbol{T}_n^m = G\boldsymbol{e}_\theta - E\boldsymbol{e}_\varphi = \nabla_{\theta,\varphi}Y_n^m \times \boldsymbol{1}_r = -\mathrm{i}\sqrt{n(n+1)}\,\boldsymbol{Y}_{n,n}^m. \qquad (A13c)$$

We can transform between the components of vectors in the rank 1 tensor spherical harmonics basis, $(u_{n,n-1}^m, u_{n,n}^m, u_{n,n+1}^m)$, and in the scaloidal-poloidal-toroidal basis, (U_n^m, V_n^m, W_n^m), as

$$U_n^m = \frac{1}{\sqrt{2n+1}}[\sqrt{n}\,u_{n,n-1}^n - \sqrt{n+1}\,u_{n,n+1}^n], \qquad (A14a)$$

$$V_n^m = \frac{1}{\sqrt{2n+1}}\left[\frac{u_{n,n-1}^n}{\sqrt{n}} + \frac{u_{n,n+1}^n}{\sqrt{n+1}}\right], \qquad (A14b)$$

$$W_n^m = \frac{\mathrm{i}}{\sqrt{n(n+1)}}u_{n,n}^m, \qquad (A14c)$$

or in matrix form as

$$\boldsymbol{U}_n^m = \boldsymbol{C}_{u\to U}\boldsymbol{u}_{n,n_1}^m, \qquad (A15)$$

where we have introduced $\boldsymbol{u}_{n,n_1}^m = (...u_{n,n-1}^m, u_{n,n}^m, u_{n,n+1}^m...)^\dagger$ and $\boldsymbol{U}_n^m = (...U_n^m, V_n^m, W_n^m...)^\dagger$

A.4. Rank 2 Tensors

A rank 2 tensor ($\boldsymbol{A}$) can be expanded into tensor spherical harmonics of rank 2, $\boldsymbol{A} = \sum_{n,m,n_1,n_2} A_{n,n_1,n_2}^m \boldsymbol{Y}_{n,n_1,n_2}^m$, which in spherical coordinates are given by

$$\sqrt{n(n-1)(2n-1)(2n+1)}\,\boldsymbol{Y}_{n,n-1,n-2}^m = n(n-1)Y\boldsymbol{e}_r\boldsymbol{e}_r + (n-1)E\boldsymbol{e}_r\boldsymbol{e}_\theta + (n-1)G\boldsymbol{e}_r\boldsymbol{e}_\varphi + (n-1)E\boldsymbol{e}_\theta\boldsymbol{e}_r$$
$$+(nY+F)\boldsymbol{e}_\theta\boldsymbol{e}_\theta + H\boldsymbol{e}_\theta\boldsymbol{e}_\varphi + (n-1)G\boldsymbol{e}_\varphi\boldsymbol{e}_r + H\boldsymbol{e}_\varphi\boldsymbol{e}_\theta - (F+n^2Y)\boldsymbol{e}_\varphi\boldsymbol{e}_\varphi \qquad (A16a)$$

$$\mathrm{i}n\sqrt{(n-1)(2n+1)}\,\boldsymbol{Y}_{n,n-1,n-1}^m = (1-n)G\boldsymbol{e}_\theta\boldsymbol{e}_r - H\boldsymbol{e}_\theta\boldsymbol{e}_\theta + (F+n^2Y)\boldsymbol{e}_\theta\boldsymbol{e}_\varphi$$
$$+(n-1)E\boldsymbol{e}_\varphi\boldsymbol{e}_r + (F+nY)\boldsymbol{e}_\varphi\boldsymbol{e}_\theta + H\boldsymbol{e}_\varphi\boldsymbol{e}_\varphi \qquad (A16b)$$

$$n\sqrt{4n^2-1}\,\boldsymbol{Y}_{n,n-1,n}^m = -n^2Y\boldsymbol{e}_r\boldsymbol{e}_r - nE\boldsymbol{e}_r\boldsymbol{e}_\theta - nG\boldsymbol{e}_r\boldsymbol{e}_\varphi + (n-1)E\boldsymbol{e}_\theta\boldsymbol{e}_r + (nY+F)\boldsymbol{e}_\theta\boldsymbol{e}_\theta$$
$$+H\boldsymbol{e}_\theta\boldsymbol{e}_\varphi + (n-1)G\boldsymbol{e}_\varphi\boldsymbol{e}_r + H\boldsymbol{e}_\varphi\boldsymbol{e}_\theta - (F+n^2Y)\boldsymbol{e}_\varphi\boldsymbol{e}_\varphi \qquad (A16c)$$

$$\mathrm{i}n\sqrt{(2n+1)(n+1)}\,\boldsymbol{Y}_{n,n,n-1}^m = -nG\boldsymbol{e}_r\boldsymbol{e}_\theta + nE\boldsymbol{e}_r\boldsymbol{e}_\varphi + G\boldsymbol{e}_\theta\boldsymbol{e}_r$$
$$-H\boldsymbol{e}_\theta\boldsymbol{e}_\theta + F\boldsymbol{e}_\theta\boldsymbol{e}_\varphi - E\boldsymbol{e}_\varphi\boldsymbol{e}_r + (F+n(n+1)Y)\boldsymbol{e}_\varphi\boldsymbol{e}_\theta + H\boldsymbol{e}_\varphi\boldsymbol{e}_\varphi \qquad (A16d)$$

$$n(n+1)Y_{n,n,n}^m = -Ee_\theta e_r + (F + n(n+1))e_\theta e_\theta + He_\theta e_\varphi - Ge_\varphi e_r + He_\varphi e_\theta - Fe_\varphi e_\varphi \tag{A16e}$$

$$i(n+1)\sqrt{n(2n+1)}\,Y_{n,n,n+1}^m = (n+1)Ge_r e_\theta - (n+1)Ee_r e_\varphi + Ge_\theta e_r$$
$$-He_\theta e_\theta + Fe_\theta e_\varphi - Ee_\varphi e_r + (F+n(n+1)Y)e_\varphi e_\theta + He_\varphi e_\varphi \tag{A16f}$$

$$(n+1)\sqrt{(2n+3)(2n+1)}\,Y_{n,n+1,n}^m = -(n+1)^2 Ye_r e_r + (n+1)Ee_r e_\theta + (n+1)Ge_r e_\varphi - (n+2)Ee_\theta e_r$$
$$+(F-(n+1)Y)e_\theta e_\theta + He_\theta e_\varphi - (n+2)Ge_\varphi e_r + He_\varphi e_\theta - (F+(n+1)^2)e_\varphi e_\varphi \tag{A16g}$$

$$i(n+1)\sqrt{(n+2)(2n+1)}\,Y_{n,n+1,n+1}^m = (n+2)Ge_\theta e_r - He_\theta e_\theta + (F+(n+1)^2)Ye_\theta e_\varphi$$
$$-(n+2)Ee_\varphi e_r + (F-(n+1)Y)e_\varphi e_\theta + He_\varphi e_\varphi \tag{A16h}$$

$$\sqrt{(n+1)(n+2)(2n+1)(2n+3)}\,Y_{n,n+1,n+2}^m = (n+1)(n+2)Ye_r e_r - (n+2)Ee_r e_\theta - (n+2)Ge_r e_\varphi$$
$$-(n+2)Ee_\theta e_r + (F-(n+1)Y)e_\theta e_\theta + He_\theta e_\varphi - (n+2)Ge_\varphi e_r + He_\varphi e_\theta - (F+(n+1)^2 Y)e_\varphi e_\varphi. \tag{A16i}$$

Alternatively, rank 2 tensors can be expanded using Zerilli tensors, $\boldsymbol{A} = \sum_{n,m,l,n_2} A_{n,n_2;m}^{(l)} \boldsymbol{T}_{n,n_2;m}^{(l)}$, which are linearly related to rank 2 tensor spherical harmonics as

$$\boldsymbol{T}_{n,n_2;m}^{(l)} = \sum_{n_1} (-1)^{n+n_2+l} \Lambda(n_1, l) \begin{Bmatrix} 1 & l & 1 \\ n & n_1 & n_2 \end{Bmatrix} \boldsymbol{Y}_{n,n_1,n_2}^m. \tag{A17}$$

The terms between curly brackets are Wigner's 6-j symbols. As Zerilli tensors are obtained by an unitary transformation from tensor spherical harmonics, it follows that they are also orthonormal with respect to the inner product. We can transform between the components of a tensor in tensor spherical harmonics, A_{n,n_1,n_2}^m, and in the Zerilli basis, $A_{n,n_2;m}^{(l)}$, as

$$A_{n,n_1,n_2}^m = \sum_l (-1)^{n+n_2+l} \Lambda(n_1, l) \begin{Bmatrix} 1 & l & 1 \\ n & n_1 & n_2 \end{Bmatrix} A_{n,n_2;m}^{(l)}. \tag{A18}$$

A.5. Operators

The following operators are used:

$$\partial_n^{n'} = \begin{cases} \partial_r + \dfrac{n+1}{r}, & \text{if } n = n'+1 \\ \partial_r - \dfrac{n}{r}, & \text{if } n = n'-1 \end{cases} \tag{A19a}$$

$$G(n_k, n_{k+1}) = (-1)^{n_k} \Lambda(n_{k+1}) \begin{pmatrix} n_k & n_{k+1} & 1 \\ 0 & 0 & 0 \end{pmatrix} = \frac{1}{\sqrt{2n_k+1}} \begin{cases} \sqrt{n_k}, & \text{if } n_{k+1} = n_k - 1 \\ -\sqrt{n_k+1}, & \text{if } n_{k+1} = n_k + 1 \\ 0, & \text{if otherwise} \end{cases} \tag{A19b}$$

$$D_n = \partial_r^2 + \frac{2}{r}\partial_r - \frac{n(n+1)}{r^2}. \tag{A20}$$

Appendix B
Tensor Spherical Harmonics Integrals

To obtain both the coupling coefficients and the energy dissipation spectra, the following integral should be evaluated:

$$(\boldsymbol{T}_{n_\alpha,n_{2\alpha};m_\alpha}^{(l_\alpha)} : \overline{\boldsymbol{T}_{n_\beta,n_{2\beta};m_\beta}^{(l_\beta)}} \cdot Y_{n_\nu}^{m_\nu}) = \frac{1}{4\pi} \int \boldsymbol{T}_{n_\alpha,n_{2\alpha};m_\alpha}^{(l_\alpha)} : \overline{\boldsymbol{T}_{n_\beta,n_{2\beta};m_\beta}^{(l_\beta)}} \; Y_{n_\nu}^{m_\nu} d\Omega, \tag{B1a}$$

$$(\boldsymbol{T}_{n_\alpha,n_{2\alpha};m_\alpha}^{(l_\alpha)} : \boldsymbol{T}_{n_\beta,n_{2\beta};m_\beta}^{(l_\beta)} \cdot \overline{Y_{n_\nu}^{m_\nu}}) = \frac{1}{4\pi} \int \boldsymbol{T}_{n_\alpha,n_{2\alpha};m_\alpha}^{(l_\alpha)} : \boldsymbol{T}_{n_\beta,n_{2\beta};m_\beta}^{(l_\beta)} \overline{Y_{n_\nu}^{m_\nu}} d\Omega. \tag{B1b}$$

Equation (B1a)) is required to compute the coupling coefficients and (B1b) to compute the energy dissipation integrals. The two expressions can be obtained from

$$(\boldsymbol{T}_{n_\alpha,n_{2\alpha};m_\alpha}^{(l_\alpha)} : \boldsymbol{T}_{n_\beta,n_{2\beta};m_\beta}^{(l_\beta)} \cdot Y_{n_\nu}^{m_\nu}) = \frac{1}{4\pi} \int \boldsymbol{T}_{n_\alpha,n_{2\alpha};m_\alpha}^{(l_\alpha)} : \boldsymbol{T}_{n_\beta,n_{2\beta};m_\beta}^{(l_\beta)} \; Y_{n_\nu}^{m_\nu} d\Omega, \tag{B2}$$

using the complex-conjugate properties of tensor spherical harmonics (Equation (A7)). To evaluate $(\boldsymbol{T}^{(l_\alpha)}_{n_\alpha,n_{2\alpha};m_\alpha} : \boldsymbol{T}^{(l_\beta)}_{n_\beta,n_{2\beta};m_\beta} \cdot Y^{m_\nu}_{n_\nu})$, we write it in terms of rank 2 spherical harmonics $Y^m_{n(2)}$ (Equation (A17)):

$$(\boldsymbol{T}^{(l_\alpha)}_{n_\alpha,n_{2\alpha},m_\alpha} : \boldsymbol{T}^{(l_\beta)}_{n_\beta,n_{2\beta};m_\beta} \cdot Y^{m_\nu}_{n_\nu}) = (-1)^{n_\alpha+n_{2\alpha}+l_\alpha+n_\beta+n_{2\beta}+l_\beta}$$

$$\sum_{n_{1\alpha},n_{1\beta}} \Lambda(n_{1\alpha}, n_{1\beta}, l_\alpha, l_\beta) \begin{Bmatrix} 1 & l_\beta & 1 \\ n_\beta & n_{1\beta} & n_{2\beta} \end{Bmatrix} \begin{Bmatrix} 1 & l_\alpha & 1 \\ n_\alpha & n_{1\alpha} & n_{2\alpha} \end{Bmatrix} \frac{1}{4\pi} \int Y_{n_\alpha(2)} : Y_{n_\beta(2)} Y^{m_\nu}_{n_\nu} d\Omega, \tag{B3}$$

which can be obtained using the expressions provided in Section 4 of James & Cook (1976):

$$\frac{1}{4\pi} \int Y_{n_\alpha(2)} : Y_{n_\beta(2)} Y^{m_\nu}_{n_\nu} d\Omega$$

$$= (-1)^{n_{2\beta}+n_{1\beta}+n_{1\alpha}+n_\alpha} \Lambda(n_\alpha(2), n_\beta(2), n_\nu) \begin{pmatrix} n_{2\alpha} & n_{2\beta} & n_\nu \\ 0 & 0 & 0 \end{pmatrix} \begin{pmatrix} n_\alpha & n_\beta & n_\nu \\ m_\alpha & m_\beta & m_\nu \end{pmatrix} \begin{Bmatrix} n_\alpha & n_{1\alpha} & 1 \\ n_{1\beta} & n_\beta & n_\nu \end{Bmatrix} \begin{Bmatrix} n_{1\alpha} & n_{2\alpha} & 1 \\ n_{2\beta} & n_{1\beta} & n_\nu \end{Bmatrix}. \tag{B4}$$

We have used the abbreviation $\Lambda(n(k)) = \sqrt{(2n+1)(2n_1+1) \dots (2n_k+1)}$.

The amount of integrals that need to be evaluated is greatly reduced by noting that many are 0. $(\boldsymbol{T}^{(l_\alpha)}_{n_\alpha,n_{2\alpha},m_\alpha} : \boldsymbol{T}^{(l_\beta)}_{n_\beta,n_{2\beta};m_\beta} \cdot Y^{m_\nu}_{n_\nu})$ is 0 unless

1. $l_\alpha = l_\beta$;
2. n_α, n_β, and n_ν satisfy the triangular inequality ($|n_\alpha - n_\beta| \leqslant n_\nu \leqslant n_\alpha + n_\beta$);
3. $n_{2\alpha}$, $n_{2\beta}$, and n_ν satisfy the triangular inequality;
4. $n_{2\alpha} + n_{2\beta} + n_\nu$ is even;
5. If $m_\alpha = m_\beta = m_\nu$, $n_\alpha + n_\beta + n_\nu$ is even;
6. $m_\beta + m_\alpha + m_\nu = 0$.

The previous set of properties can be used to deduce a set of selection rules for the excited modes. A mode of degree and orders (n_0, m_0), together with lateral variations of degree and order (n_1, m_1), results in modes of degree (n_2, m_2) if

$$(n_0, m_0)^x \otimes (n_1, m_1) \Rightarrow (n_2, m_2)^x \quad n_2 \in \mathcal{N}_1 \quad m_2 = m_0 + m_1$$

$$(n_0, m_0)^x \otimes (n_1, m_1) \Rightarrow (n_2, m_2)^y \quad n_2 \in \mathcal{N}_2 \quad m_2 = m_0 + m_1, \quad |m_0| + |m_1| + |m_2| \neq 0$$

$$\mathcal{N}_1: n_2 = |n_0 - n_1| + 2i, \quad 0 \leqslant i \leqslant \frac{1}{2}(n_0 + n_1 - |n_0 - n_1|)$$

$$\mathcal{N}_2: n_2 = |n_0 - n_1| + 2i + 1, \quad 0 \leqslant i \leqslant \frac{1}{2}(n_0 + n_1 - |n_0 - n_1|) - 1 \tag{B5}$$

where x or y indicate if the mode is spheroidal or toroidal, and the cases $x = s$, $y = t$, and $x = t$, $y = s$ can be considered.

Appendix C
Explicit Form of the Equations

The components of the strain tensor follow from the gradient of the displacement vector (Equation (19)):

$$\epsilon^{(0)}_{n,n;m} = -\frac{1}{\sqrt{3}} \chi^m_n, \tag{C1a}$$

$$\epsilon^{(2)}_{n,n-2;m} = \sqrt{\frac{n-1}{2n-1}} \left(\partial_r u^m_{n,n-1} + \frac{n}{r} u^m_{n,n-1} \right), \tag{C1b}$$

$$\epsilon^{(2)}_{n,n-1;m} = \frac{1}{\sqrt{2}} \sqrt{\frac{n-1}{2n+1}} \left(\partial_r u^m_{n,n} + \frac{n+1}{r} u^m_{n,n} \right), \tag{C1c}$$

$$\epsilon^{(2)}_{n,n;m} = -\sqrt{\frac{(2n+3)(2n+2)}{12(2n-1)(2n+1)}} \left(\partial_r - \frac{n-1}{r} \right) u^m_{n,n-1,n} + \sqrt{\frac{n(2n-1)(n+1)}{3(2n+3)(2n+2)(2n+1)}} \left(\partial_r + \frac{n+2}{r} \right) u^m_{n,n+1,n}, \tag{C1d}$$

$$\epsilon^{(2)}_{n,n+1;m} = -\frac{1}{\sqrt{2}} \sqrt{\frac{n+2}{2n+1}} \left(\partial_r u^m_{n,n} - \frac{n}{r} u^m_{n,n} \right), \tag{C1e}$$

$$\epsilon^{(2)}_{n,n+2;m} = -\sqrt{\frac{n+2}{2n+3}} \left(\partial_r u^m_{n,n+1} - \frac{n+1}{r} u^m_{n,n+1} \right). \tag{C1f}$$

χ_n^m is the divergence of the displacement vector:

$$\chi_n^m = \frac{1}{\sqrt{2n+1}}\left[\sqrt{n}\,\partial_r u_{n,n-1}^m - \sqrt{n+1}\,\partial_r u_{n,n+1}^m - \frac{1}{r}((n-1)\sqrt{n}\,u_{n,n-1}^m + \sqrt{n+1}\,(n+2)u_{n,n+1}^m)\right]$$

$$= \partial_r U_n^m + \frac{2U_n^m}{r} - \frac{n(n+1)}{r}V_n^m. \tag{C2}$$

Equation (C1) can be written more concisely as

$$\epsilon_{n,n_2,m}^{(l)} = \left(\boldsymbol{E}_{\partial_r}\partial_r + \frac{\boldsymbol{E}}{r}\right)\boldsymbol{u}_{n,n_1}^m, \tag{C3}$$

with $\epsilon_{n,n_2,m}^{(l)}$ being a vector containing the elements of the strain tensor, $\epsilon_{n,n_2,m}^{(l)} = (\dots \epsilon_{n,n,m}^{(0)},\ \epsilon_{n,n-2,m}^{(2)}\epsilon_{n,n-1,m}^{(2)},\ \epsilon_{n,n,m}^{(2)},\ \epsilon_{n,n+1,m}^{(2)},\ \epsilon_{n,n+2,m}^{(2)}\dots)^\dagger$.

The components of the stress tensor can be written in terms of the strain tensor and the material properties:

$$\sigma_{n,n;m}^{(0)} = 3\kappa_0\,\epsilon_{n,n;m}^{(0)} + 3\kappa_0 \sum_{\substack{n_\beta,m_\beta,\\ n_\alpha,m_\alpha}} \kappa_{n_\beta}^{m_\beta}\epsilon_{n_\alpha,n_\alpha;m_\alpha}^{(0)}(\boldsymbol{T}_{n_\alpha,n_\alpha;m_\alpha}^{(0)}:\overline{\boldsymbol{T}_{n,n;m}^{(0)}} \cdot Y_{n_\beta}^{m_\beta}), \tag{C4a}$$

$$\sigma_{n,n_2;m}^{(2)} = 2\hat{\mu}_0\,\epsilon_{n,n_2;m}^{(2)} + 2\mu_0 \sum_{\substack{n_\beta,m_\beta,\\ n_\alpha,m_\alpha,n_{2\alpha}}} \hat{\mu}_{n_\beta}^{m_\beta}\epsilon_{n_\alpha,n_{2\alpha};m_\alpha}^{(2)}(\boldsymbol{T}_{n_\alpha,n_{2\alpha};m_\alpha}^{(2)}:\overline{\boldsymbol{T}_{n,n_2;m}^{(2)}} \cdot Y_{n_\beta}^{m_\beta}), \tag{C4b}$$

or in matrix form as

$$\boldsymbol{\sigma}_{n,n_2,m}^{(l)} = (\boldsymbol{R}_u + \boldsymbol{R}_v)\,\epsilon_{n,n_2,m}^{(l)}, \tag{C5}$$

with $\boldsymbol{\sigma}_{n,n_2,m}^{(l)}$ being a vector containing the components of the stress tensor, $\boldsymbol{\sigma}_{n,n_2,m}^{(l)} = (\dots\sigma_{n,n,m}^{(0)},\ \sigma_{n,n-2,m}^{(2)}\sigma_{n,n-1,m}^{(2)},\ \sigma_{n,n,m}^{(2)},\ \sigma_{n,n+1,m}^{(2)},\ \sigma_{n,n+2,m}^{(2)}\dots)^\dagger$; $\boldsymbol{R}_u$ a matrix with the mean mechanical properties of the material,

$$\boldsymbol{R}_u = \begin{bmatrix} (\boldsymbol{R}_u)_{0,0} & & \\ & \ddots & \\ & & (\boldsymbol{R}_u)_{\infty,\infty} \end{bmatrix} \tag{C6a}$$

$$(\boldsymbol{R}_u)_{n,m} = \mathrm{diag}(3\kappa_0,\ 2\hat{\mu}_0,\ 2\hat{\mu}_0,\ 2\hat{\mu}_0,\ 2\hat{\mu}_0,\ 2\hat{\mu}_0), \tag{C6b}$$

and $\boldsymbol{R}_v$ a matrix that includes both the lateral variations of mechanical properties of the material and the coupling coefficients,

$$\boldsymbol{R}_v = \begin{bmatrix} (\boldsymbol{R}_v)_{0,0}^{0,0} & \cdots & (\boldsymbol{R}_v)_{0,0}^{\infty,\infty} \\ \vdots & \ddots & \vdots \\ (\boldsymbol{R}_v)_{\infty,\infty}^{0,0} & \cdots & (\boldsymbol{R}_v)_{\infty,\infty}^{\infty,\infty} \end{bmatrix} \tag{C7a}$$

$$(\boldsymbol{R}_v)_{n,m}^{n_\alpha,m_\alpha} = \sum_{n_\beta,m_\beta} \boldsymbol{R}_{n_\beta,m_\beta}\ \underset{n_\beta,m_\beta}{\mathbf{C}}\ {}_{n,m}^{n_\alpha,m_\alpha} \tag{C7b}$$

$$\boldsymbol{R}_{n_\beta,m_\beta} = \mathrm{diag}(3\kappa_0\kappa_{n_\beta}^{m_\beta},\ 2\mu_0\hat{\mu}_{n_\beta}^{m_\beta},\ 2\mu_0\hat{\mu}_{n_\beta}^{m_\beta},\ 2\mu_0\hat{\mu}_{n_\beta}^{m_\beta},\ 2\mu_0\hat{\mu}_{n_\beta}^{m_\beta},\ 2\mu_0\hat{\mu}_{n_\beta}^{m_\beta}) \tag{C7c}$$

$$\underset{n_\beta,m_\beta}{\mathbf{C}}\,{}_{n,m}^{n_\alpha,m_\alpha} = \begin{bmatrix} \underset{n_\beta,m_\beta}{C^{(0)}}{}_{n,n,m}^{n_\alpha,n_\alpha,m_\alpha} & 0 & 0 & 0 & 0 & 0 \\[1.2em] 0 & \underset{n_\beta,m_\beta}{C^{(2)}}{}_{n,n-2,m}^{n_\alpha,n_\alpha-2,m_\alpha} & \underset{n_\beta,m_\beta}{C^{(2)}}{}_{n,n-2,m}^{n_\alpha,n_\alpha-1,m_\alpha} & \underset{n_\beta,m_\beta}{C^{(2)}}{}_{n,n-2,m}^{n_\alpha,n_\alpha,m_\alpha} & \underset{n_\beta,m_\beta}{C^{(2)}}{}_{n,n-2,m}^{n_\alpha,n_\alpha+1,m_\alpha} & \underset{n_\beta,m_\beta}{C^{(2)}}{}_{n,n-2,m}^{n_\alpha,n_\alpha+2,m_\alpha} \\[1.2em] 0 & \underset{n_\beta,m_\beta}{C^{(2)}}{}_{n,n-1,m}^{n_\alpha,n_\alpha-2,m_\alpha} & \underset{n_\beta,m_\beta}{C^{(2)}}{}_{n,n-1,m}^{n_\alpha,n_\alpha-1,m_\alpha} & \underset{n_\beta,m_\beta}{C^{(2)}}{}_{n,n-1,m}^{n_\alpha,n_\alpha,m_\alpha} & \underset{n_\beta,m_\beta}{C^{(2)}}{}_{n,n-1,m}^{n_\alpha,n_\alpha+1,m_\alpha} & \underset{n_\beta,m_\beta}{C^{(2)}}{}_{n,n-1,m}^{n_\alpha,n_\alpha+2,m_\alpha} \\[1.2em] 0 & \underset{n_\beta,m_\beta}{C^{(2)}}{}_{n,n,m}^{n_\alpha,n_\alpha-2,m_\alpha} & \underset{n_\beta,m_\beta}{C^{(2)}}{}_{n,n,m}^{n_\alpha,n_\alpha-1,m_\alpha} & \underset{n_\beta,m_\beta}{C^{(2)}}{}_{n,n,m}^{n_\alpha,n_\alpha,m_\alpha} & \underset{n_\beta,m_\beta}{C^{(2)}}{}_{n,n,m}^{n_\alpha,n_\alpha+1,m_\alpha} & \underset{n_\beta,m_\beta}{C^{(2)}}{}_{n,n,m}^{n_\alpha,n_\alpha+2,m_\alpha} \\[1.2em] 0 & \underset{n_\beta,m_\beta}{C^{(2)}}{}_{n,n+1,m}^{n_\alpha,n_\alpha-2,m_\alpha} & \underset{n_\beta,m_\beta}{C^{(2)}}{}_{n,n+1,m}^{n_\alpha,n_\alpha-1,m_\alpha} & \underset{n_\beta,m_\beta}{C^{(2)}}{}_{n,n+1,m}^{n_\alpha,n_\alpha,m_\alpha} & \underset{n_\beta,m_\beta}{C^{(2)}}{}_{n,n+1,m}^{n_\alpha,n_\alpha+1,m_\alpha} & \underset{n_\beta,m_\beta}{C^{(2)}}{}_{n,n+1,m}^{n_\alpha,n_\alpha+2,m_\alpha} \\[1.2em] 0 & \underset{n_\beta,m_\beta}{C^{(2)}}{}_{n,n+2,m}^{n_\alpha,n_\alpha-2,m_\alpha} & \underset{n_\beta,m_\beta}{C^{(2)}}{}_{n,n+2,m}^{n_\alpha,n_\alpha-1,m_\alpha} & \underset{n_\beta,m_\beta}{C^{(2)}}{}_{n,n+2,m}^{n_\alpha,n_\alpha,m_\alpha} & \underset{n_\beta,m_\beta}{C^{(2)}}{}_{n,n+2,m}^{n_\alpha,n_\alpha+1,m_\alpha} & \underset{n_\beta,m_\beta}{C^{(2)}}{}_{n,n+2,m}^{n_\alpha,n_\alpha+2,m_\alpha} \end{bmatrix}, \tag{C7d}$$

where we have introduced the notation $\underset{n_\beta,m_\beta}{C^{(l)}}{}_{n,n_2,m}^{n_\alpha,n_{2\alpha},m_\alpha} = (\boldsymbol{T}_{n_\alpha,n_{2\alpha};m_\alpha}^{(l)}:\overline{\boldsymbol{T}_{n,n_2;m}^{(l)}} \cdot Y_{n_\beta}^{m_\beta})$. $\boldsymbol{R}_{n_\beta,m_\beta}$ contains the mechanical properties, and $\underset{n_\beta,m_\beta}{\mathbf{C}}\,{}_{n,m}^{n_\alpha,m_\alpha}$ is a matrix with the coupling coefficients. If there are no lateral variations, $\boldsymbol{R}_v$ is 0.

The explicit forms of the momentum (Equation (16)) and Poisson equations (Equation (17)) are

$$-\sqrt{\frac{n}{6n+3}}\left(\partial_r + \frac{n+1}{r}\right)\sigma_{n,n;m}^{(0)} - \sqrt{\frac{(2n+3)(2n+2)}{12(2n-1)(2n+1)}}\left(\partial_r + \frac{n+1}{r}\right)\sigma_{n,n;m}^{(2)}$$

$$+\sqrt{\frac{n-1}{2n-1}}\left(\partial_r - \frac{n-2}{r}\right)\sigma_{n,n-2;m}^{(2)} - \rho_0\frac{n}{2n+1}\left(\partial_r g + \frac{2n}{r}g\right)u_{n,n-1}^m + \rho_0\frac{\sqrt{n(n+1)}}{2n+1}\left(\partial_r g - \frac{g}{r}\right)u_{n,n+1}^m - \rho_0\sqrt{\frac{n}{2n+1}}\left(\partial_r + \frac{n+1}{r}\right)\phi_n^m = 0 \qquad (\text{C8a})$$

$$\sqrt{\frac{n+1}{6n+3}}\left(\partial_r - \frac{n}{r}\right)\sigma_{n,n;m}^{(0)} + \sqrt{\frac{n(n+1)(2n-1)}{3(2n+1)(2n+2)(2n+3)}}\left(\partial_r - \frac{n}{r}\right)\sigma_{n,n;m}^{(2)} - \sqrt{\frac{n+2}{2n+3}}\left(\partial_r + \frac{n+3}{r}\right)\sigma_{n,n+2;m}^{(2)}$$

$$+\rho_0\frac{\sqrt{n(n+1)}}{2n+1}\left(\partial_r g - \frac{g}{r}\right)u_{n,n-1}^m + \rho_0\frac{n+1}{2n+1}\left(-\partial_r g + g\frac{2n+2}{r}\right)u_{n,n+1}^m + \rho_0\sqrt{\frac{n+1}{2n+1}}\left(\partial_r - \frac{n}{r}\right)\phi_n^m = 0 \qquad (\text{C8b})$$

$$\sqrt{n-1}\left(\partial_r - \frac{n-1}{r}\right)\sigma_{n,n-1;m}^{(2)} - \sqrt{n+2}\left(\partial_r + \frac{n+2}{r}\right)\sigma_{n,n+1;m}^{(2)} = 0 \qquad (\text{C8c})$$

$$\left(\partial_r^2 + \frac{2\partial_r}{r} - \frac{n(n+1)}{r^2}\right)\phi_n^m = -4\pi G\left[\sqrt{\frac{n}{2n+1}}\left(\rho_0\partial_r + \partial_r\rho_0 - \rho_0\frac{n-1}{r}\right)u_{n,n-1}^m - \sqrt{\frac{n+1}{2n+1}}\left(\rho_0\partial_r + \partial_r\rho_0 + \rho_0\frac{n+2}{r}\right)u_{n,n+1}^m\right]. \qquad (\text{C8d})$$

To cast the governing equations in terms of U_n^m, V_n^m, W_n^m, R_n^m, S_n^m, T_n^m, ϕ_n^m, $\partial_r\phi_n^m$, and their derivatives, we first need to obtain the radial components of the stress tensor (James & Cook 1976, Equation (3.22)),

$$R_n^m = -\frac{1}{\sqrt{3}}\sigma_{n,n;m}^{(0)} - \frac{\sqrt{n}}{2n+1}\left(\sqrt{\frac{(2n+3)(2n+2)}{12(2n-1)}} + \sqrt{\frac{(2n-1)(n+1)^2}{3(2n+2)(2n+3)}}\right)\sigma_{n,n;m}^{(2)} + \sqrt{\frac{n(n-1)}{(2n-1)(2n+1)}}\sigma_{n,n-2;m}^{(2)} + \sqrt{\frac{(n+1)(n+2)}{(2n+1)(2n+3)}}\sigma_{n,n+2;m}^{(2)} = \boldsymbol{C}_{\sigma\to R_n^m}\boldsymbol{\sigma}_{n,n_2,m}^{(l)} \qquad (\text{C9a})$$

$$S_n^m = \frac{1}{\sqrt{2n+1}}\left[\left(-\sqrt{\frac{(2n+3)(2n+2)}{(12n(2n-1)(2n+1))}} + \sqrt{\frac{n(2n-1)}{3(2n+1)(2n+2)(2n+3)}}\right)\sigma_{n,n;m}^{(2)} + \sqrt{\frac{n-1}{(2n-1)n}}\sigma_{n,n-2;m}^{(2)} - \sqrt{\frac{n+2}{(2n+3)(n+1)}}\sigma_{n,n+2;m}^{(2)}\right] = \boldsymbol{C}_{\sigma\to S_n^m}\boldsymbol{\sigma}_{n,n_2,m}^{(l)} \qquad (\text{C9b})$$

$$T_n^m = \frac{\mathrm{i}}{\sqrt{2n(n+1)(2n+1)}}\left[\sqrt{n-1}\,\sigma_{n,n-1;m}^{(2)} - \sqrt{n+2}\,\sigma_{n,n+1;m}^{(2)}\right] = \boldsymbol{C}_{\sigma\to T_n^m}\boldsymbol{\sigma}_{n,n_2,m}^{(l)}, \qquad (\text{C9c})$$

and then project the momentum equation to the scaloidal-poloidal-toroidal basis:

$$-\partial_r R_n^m = \frac{1}{2n+1}\left[-(n+1)\sqrt{\frac{(2n+3)(2n+2)n}{12(2n-1)}} + n\sqrt{\frac{n(n+1)^2(2n-1)}{3(2n+2)(2n+3)}}\right]\frac{\sigma_{n,n;m}^{(2)}}{r} - (n-2)\sqrt{\frac{n(n-1)}{(2n-1)(2n+1)}}\frac{\sigma_{n,n-2;m}^{(2)}}{r}$$

$$+(n+3)\sqrt{\frac{(n+1)(n+2)}{(2n+3)(2n+1)}}\frac{\sigma_{n,n+2;m}^{(2)}}{r} - \rho_0\partial_r\phi_n^m + \rho g\chi_n^m - \rho\partial_r(gU_n^m) = \frac{\boldsymbol{C}_{\sigma\to\partial_r R_n^m}}{r}\boldsymbol{\sigma}_{n,n_2,m}^{(l)} - \rho_0\partial_r\phi_n^m - \rho g\chi_n^m - \rho\partial_r(gU_n^m) \qquad (\text{C10a})$$

$$-\partial_r S_n^m = -\frac{1}{\sqrt{3}}\frac{\sigma_{n,n;m}^{(0)}}{r} - \frac{1}{2n+1}\left[(n+1)\sqrt{\frac{(2n+3)(2n+2)}{12n(2n-1)}} + n\sqrt{\frac{n(2n-1)}{3(2n+2)(2n+3)}}\right]\frac{\sigma_{n,n;m}^{(2)}}{r} - (n-2)\sqrt{\frac{(n-1)}{(2n-1)(2n+1)n}}\frac{\sigma_{n,n-2;m}^{(2)}}{r}$$

$$- (n+3)\sqrt{\frac{(n+2)}{(2n+3)(2n+1)(n+1)}}\frac{\sigma_{n,n+2;m}^{(2)}}{r} - \frac{\rho}{r}\phi_n^m - \frac{\rho g}{r}U_n^m = \frac{\boldsymbol{C}_{\sigma\to\partial_r S_n^m}}{r}\boldsymbol{\sigma}_{n,n_2,m}^{(l)} - \frac{\rho}{r}\phi_n^m - \frac{\rho g}{r}U_n^m \qquad (\text{C10b})$$

$$\partial_r T_n^m = \frac{\mathrm{i}}{r\sqrt{2n(n+1)(2n+1)}}\left[(n-1)^{3/2}\sigma_{n,n-1;m}^{(2)} + (n+2)^{3/2}\sigma_{n,n+1;m}^{(2)}\right] = \frac{\boldsymbol{C}_{\sigma\to\partial_r T_n^m}}{r}\boldsymbol{\sigma}_{n,n_2,m}^{(l)}. \qquad (\text{C10c})$$

For conciseness, we have introduced the matrices $\boldsymbol{C}_{\sigma\to R_n^m}$, $\boldsymbol{C}_{\sigma\to S_n^m}$, $\boldsymbol{C}_{\sigma\to T_n^m}$ that allow to obtain the radial, solenoidal, and toroidal components of the radial component of the stress tensors in terms of $\boldsymbol{\sigma}_{n,n_2,m}^{(l)}$; and $\boldsymbol{C}_{\sigma\to\partial_r R_n^m}$, $\boldsymbol{C}_{\sigma\to\partial_r S_n^m}$, $\boldsymbol{C}_{\sigma\to\partial_r T_n^n}$ that can be used to write part of $\partial_r R_n^m$, $\partial_r S_n^m$ and $\partial_r T_n^m$ in terms of $\boldsymbol{\sigma}_{n,n_2,m}^{(l)}$.

Plugging the expressions for the stress tensor (Equation (C4)) into Equations (C9) and (C10), using the linear transformation between U_n^m, V_n^m, W_n^m and $u_{n,n-1}^m$, $u_{n,n}^m$, $u_{n,n+1}^m$ (Equation (A14)) for the resulting equations and Poisson's equation (Equation (C8d)),

we find

$$-\rho_0\partial_r\phi_n^m - \rho_0\partial_r(gU_n^m) + \rho_0 g\chi_n^m + \partial_r R_n^m + \frac{\hat{\mu}_0}{r^2}[4r\partial_r U_n^m - 4U_n^m + n(n+1)(3V_n^m - U_n^m - r\partial_r V_n^m)]$$

$$+\frac{\boldsymbol{C}_{\sigma\rightarrow\partial_r R_n^m}}{r}\boldsymbol{R}_v\left(\boldsymbol{E}_{\partial_r}\partial_r + \frac{\boldsymbol{E}}{r}\right)\boldsymbol{C}_{U\rightarrow u}U_n^m = 0 \tag{C11a}$$

$$-\frac{\rho_0}{r}\phi_n^m - \frac{\rho_0}{r}gU_n^m + \frac{\hat{\lambda}_0}{r}\chi_n^m + \partial_r S_n^m + \frac{\hat{\mu}_0}{r^2}[5U_n^m + 3r\partial_r V_n^m - V_n^m - 2n(n+1)V_n^m] + \frac{\boldsymbol{C}_{\sigma\rightarrow\partial_r S_n^m}}{r}\boldsymbol{R}_v\left(\boldsymbol{E}_{\partial_r}\partial_r + \frac{\boldsymbol{E}}{r}\right)\boldsymbol{C}_{U\rightarrow u}U_n^m = 0 \tag{C11b}$$

$$\partial_r T_n^m + \frac{3}{r}T_n^m - \frac{\hat{\mu}_0}{r^2}(n(n+1)-2)W_n^m + \frac{\boldsymbol{C}_{\sigma\rightarrow\partial_r T_n^m}}{r}\boldsymbol{R}_v\left(\boldsymbol{E}_{\partial_r}\partial_r + \frac{\boldsymbol{E}}{r}\right)\boldsymbol{C}_{U\rightarrow u}U_n^m = 0 \tag{C11c}$$

$$\left(\partial_r^2 + \partial_r\frac{2}{r} - \frac{n(n+1)}{r^2}\right)\phi_n^m = -4\pi G(\rho\chi_n^m + U_n^m\partial_r\rho_0) \tag{C11d}$$

$$R_n^m = \hat{\lambda}_0\chi_n^m + 2\hat{\mu}_0\partial_r U_n^m + \boldsymbol{C}_{\sigma\rightarrow R_n^m}\boldsymbol{R}_v\left(\boldsymbol{E}_{\partial_r}\partial_r + \frac{\boldsymbol{E}}{r}\right)\boldsymbol{C}_{U\rightarrow u}U_n^m \tag{C11e}$$

$$S_n^m = \hat{\mu}_0\left(\partial_r V_n^m + \frac{U_n^m - V_n^m}{r}\right) + \boldsymbol{C}_{\sigma\rightarrow S_n^m}\boldsymbol{R}_v\left(\boldsymbol{E}_{\partial_r}\partial_r + \frac{\boldsymbol{E}}{r}\right)\boldsymbol{C}_{U\rightarrow u}U_n^m \tag{C11f}$$

$$T_n^m = \hat{\mu}_0\left[\partial_r W_n^m - \frac{W_n^m}{r}\right] + \boldsymbol{C}_{\sigma\rightarrow T_n^m}\boldsymbol{R}_v\left(\boldsymbol{E}_{\partial_r}\partial_r + \frac{\boldsymbol{E}}{r}\right)\boldsymbol{C}_{U\rightarrow u}U_n^m. \tag{C11g}$$

The terms with $\boldsymbol{R}_v$ arise from lateral variations and couple equations involving different modes (see Equation (C7)). Without lateral variations, Equation (C11) reduces to the equations typical of a spherically symmetric body. Using linear algebra, the previous set of equations can be cast as $\partial_r y = \boldsymbol{D}y$.

Appendix D
Tidal Potential for a Synchronous Satellite

The tidal potential experienced by a synchronous body in an eccentric orbit of period $T = 2\pi/\omega$ is given by (e.g., Jara-Orué & Vermeersen 2011)

$$\phi^T(R) = (\phi^{(T)\,0,+}_2 Y^0_2 + \phi^{(T)\,2,+}_2 Y^2_2 + \phi^{(T)-2,+}_2 Y^{-2}_2) e^{i\omega t}$$
$$+(\phi^{(T)\,0,-}_2 Y^0_2 + \phi^{(T)-2,-}_2 Y^{-2}_2 + \phi^{(T)\,2,-}_2 Y^2_2) e^{-i\omega t} + O(e^2).$$
$$(D1)$$

The $\phi^{(T)0,+}_2$, $\phi^{(T)0,-}_2$; $\phi^{(T)2,+}_2$, $\phi^{(T)2,-}_2$; and $\phi^{(T)-2,+}_2$, $\phi^{(T)-2,-}_2$ correspond to standing, westward-propagating and eastward-propagating waves, respectively. As the tidal potential is real, we have that $\phi^{(T)\,-m,-}_n = (-1)^m \phi^{(T)\,m,+}_n$. The amplitudes of the different components of the tide are given in Table 2.

Table 2
Amplitudes of the Components of the Eccentricity Tide

Tidal Component	Amplitude
$\phi^{(T)\,0,+}_2$	$\frac{3}{4}\sqrt{\frac{1}{5}}(\omega R)^2 e$
$\phi^{(T)\,2,+}_2$	$\frac{1}{8}\sqrt{\frac{6}{5}}(\omega R)^2 e$
$\phi^{(T)\,-2,+}_2$	$-\frac{7}{8}\sqrt{\frac{6}{5}}(\omega R)^2 e$

Appendix E
Test on the Total Energy Dissipation

We test that the total energy dissipation obtained using the stress and strain tensors (Equations (29)–(34)) and considering the work done by the tidal potential (Equations (35)–(37)) is the same. We consider a viscoelastic Io that is spherically symmetric and one that has zonal degree 2 lateral viscosity variations with peak-to-peak amplitudes of 50% of the mean viscosity and compute tidal heating using Equation (34) ($\dot{E}_1$) and (37) ($\dot{E}_2$). We find excellent agreement between the total energy dissipation
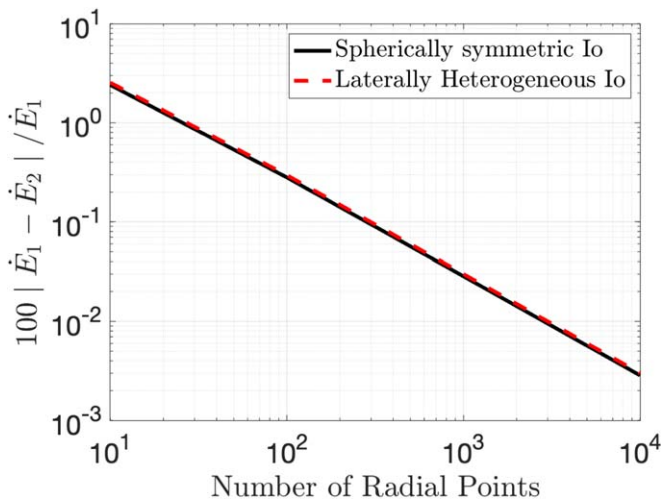

Figure 9. Difference in tidal heating computed using the stress and strain tensors (Equation (29), $\dot{E}_1$) and the work done by the tidal force (Equation (35), $\dot{E}_2$). We assume the viscoelastic Io model of Table 1 and zonal degree 2 lateral viscosity variations with peak-to-peak amplitudes of 50% of the mean viscosity.

obtained with the two methods, with the difference decreasing as the number of radial points used for the radial integration increases (Figure 9). Equivalent results are obtained for lateral variations of different amplitude, degree, and order.

ORCID iDs

Marc Rovira-Navarro ⬤ https://orcid.org/0000-0002-9980-5065
Isamu Matsuyama ⬤ https://orcid.org/0000-0002-2917-8633
Alexander Berne ⬤ https://orcid.org/0000-0001-7857-8513

References

A, G., Wahr, J., & Zhong, S. 2014, JGRE, 119, 659
Aagaard, B., Williams, C., & Knepley, M. 2007, AGUFM, T21B–0592
Alterman, Z., Jarosch, H., Pekeris, C. L., & Jeffreys, H. 1959, RSPTA, 252, 80
Altman, Y., 2024 export_fig v3.40, GitHub, https://github.com/altmany/export_fig/releases/tag/v3.40
Bêhounková, M., Souček, O., Jaroslav, H., & Čadek, O. 2017, AsBio, 17, 941
Berne, A., Simons, M., Keane, J., & Park, R. 2023a, JGRE, 128, e2022JE007712
Berne, A., Simons, M., Keane, J., & Park, R. 2023b, GeoRL, 50, e2023GL106656
Beuthe, M. 2013, Icar, 223, 308
Beuthe, M. 2018, Icar, 302, 145
Beuthe, M. 2019, Icar, 332, 66
Beuthe, M., Rivoldini, A., & Trinh, A. 2016, GeoRL, 43, 10088
Breuer, D., Hamilton, C. W., & Khurana, K. 2022, Eleme, 18, 385
Cappuccio, P., Hickey, A., Durante, D., et al. 2020, P&SS, 187, 104902
Crow-Willard, E. N., & Pappalardo, R. T. 2015, JGRE, 120, 928
Davies, A. G., Perry, J. E., Williams, D. A., & Nelson, D. M. 2024, NatAs, 8, 94
Farrell, W. E. 1972, RvGeo, 10, 761
Genova, A., Goossens, S., Mazarico, E., et al. 2019, GeoRL, 46, 3625
Genova, A., Hussmann, H., Van Hoolst, T., et al. 2021, SSRv, 217, 31
Hamilton, C. W., Beggan, C. D., Still, S., et al. 2013, E&PSL, 361, 272
Hemingway, D. J., & Mittal, T. 2019, Icar, 332, 111
Hoppa, G. V., Tufts, B. R., Greenberg, R., & Geissler, P. E. 1999, Sci, 285, 1899
Hussmann, H., Spohn, T., & Wieczerkowski, K. 2002, Icar, 156, 143
James, R. W., & Cook, A. H. 1976, RSPTA, 281, 195
Jara-Orué, H. M., & Vermeersen, B. L. 2011, Icar, 215, 417
Kang, W., & Jansen, M. 2022, ApJ, 935, 103
Kervazo, M., Tobie, G., Choblet, G., Dumoulin, C., & Behounková, M. 2021, A&A, 650, A72
Kirchoff, M. R., McKinnon, W. B., & Schenk, P. M. 2011, E&PSL, 301, 22
Konopliv, A. S., Park, R. S., Yuan, D.-N., et al. 2013, JGRE, 118, 1415
Konopliv, A. S., & Yoder, C. F. 1996, GeoRL, 23, 1857
Lainey, V., Arlot, J., Karatekin, ö., & Van Hoolst, T. 2009, Natur, 459, 957
Latychev, K., Mitrovica, J. X., Ishii, M., Chan, N.-H., & Davis, J. L. 2009, E&PSL, 277, 86
Lau, H. C., Yang, H.-Y., Tromp, J., et al. 2015, GeoJI, 202, 1392
Lau, H. C. P., Mitrovica, J. X., Davis, J. L., et al. 2017, Natur, 551, 321
Lemoine, F. G., Goossens, S., Sabaka, T. J., et al. 2013, JGRE, 118, 1676
Love, A. 1911, Some Problems of Geodynamics (Cambridge: Cambridge Univ. Press)
Love, A. E. H. 1927, A Treatise on the Mathematical Theory of Elasticity (Cambridge: Cambridge Univ. Press)
Martinec, Z. 2000, GeoJI, 142, 117
Matsuyama, I., Beuthe, M., Hay, H. C., Nimmo, F., & Kamata, S. 2018, Icar, 312, 208
Métivier, L., Greff-Lefftz, M., & Diament, M. 2006, GeoJI, 167, 1060
Métivier, L., Greff-Lefftz, M., & Diament, M. 2007, GeoJI, 168, 897
Neumann, G. A., Zuber, M. T., Smith, D. E., & Lemoine, F. G. 1996, JGR, 101, 16841
Neumann, G. A., Zuber, M. T., Wieczorek, M. A., et al. 2004, JGRE, 109, E08002
Nimmo, F., Thomas, P., Pappalardo, R., & Moore, W. 2007, Icar, 191, 183
Park, R. S., Mastrodemos, N., Jacobson, R. A., et al. 2024, JGRE, 129, e2023JE008054
Pawlowicz, R., 2020 M_Map: A mapping package for MATLAB, www.eoas.ubc.ca/~rich/map.html
Peale, S., & Cassen, P. 1978, Icar, 36, 245

Peale, S. J., Cassen, P., & Reynolds, R. T. 1979, Sci, 203, 892
Peltier, W. R. 1974, RvGeo, 12, 649
Platzman, G. W. 1984, RvGeo, 22, 73
Porco, C. C., Helfenstein, P., Thomas, P. C., et al. 2006, Sci, 311, 1393
Qin, C., 2016 Tidal-Response, GitHub, https://github.com/chinpoo/Tidal-Response
Qin, C., Zhong, S., & Wahr, J. 2014, GeoJI, 199, 631
Qin, C., Zhong, S., & Wahr, J. 2016, GeoJI, 207, 89
Renaud, J. P., & Henning, W. G. 2018, ApJ, 857, 98
Ritsema, J., Deuss, A., van Heijst, H. J., & Woodhouse, J. H. 2011, GeoJI, 184, 1223
Ross, M., & Schubert, G. 1986, JGR, 91, 447
Rovira-Navarro, M., 2024 LOV3D: A Spectral Method to Compute the Tides of Laterally Heterogenous Bodies (v1.0), 4TU.Research Data, doi:10.4121/5511f97f-04b9-479f-9e87-41dc6095a86c.v1
Rovira-Navarro, M., Matsuyama, I., & Hay, H. C. F. C. 2023, PSJ, 4, 23
Rovira-Navarro, M., Rieutord, M., Gerkema, T., et al. 2019, Icar, 321, 126
Sabadini, R., Vermeersen, B., & Cambiotti, G. 2016, Global Dynamics of the Earth: Applications of Viscoelastic Relaxation Theory to Solid-Earth and Planetary Geophysics (2nd ed.; Berlin: Springer)
Segatz, M., Spohn, T., Ross, M., & Schubert, G. 1988, Icar, 75, 187
Sohl, F., Solomonidou, A., Wagner, F. W., et al. 2014, JGRE, 119, 1013
Souček, O., Běhounková, M., Čadek, O., et al. 2019, Icar, 328, 218
Souček, O., Hron, J., Běhounková, M., & Čadek, O. 2016, GeoRL, 43, 7417
Sovkov, V., 2024 Wigner 3j-6j-9j, MATLAB Central File Exchange, https://www.mathworks.com/matlabcentral/fileexchange/74069-wigner-3j-6j-9j
Steinbrüugge, G., Padovan, S., Hussmann, H., et al. 2018, JGRE, 123, 2760
Steinke, T. 2021, PhD thesis, Delft Univ. of Tech.
Steinke, T., Hu, H., Höning, D., van der Wal, W., & Vermeersen, B. 2020a, Icar, 335, 113299
Steinke, T., Rovira-Navarro, M., van der Wal, W., & Vermeersen, B. 2021, The Tidal-Heating-Rheology Feedback in Io's Asthenosphere, The Curious Case of Io—Connections Between Interior Structure Tidal Heating and Volcanism (Delft: Delft Univ. of Tech.), 61
Steinke, T., van Sliedregt, D., Vilella, K., van der Wal, W., & Vermeersen, B. 2020b, JGRE, 125, e2020JE006521
Takeuchi, H., Saito, M., & Kobayashi, N. 1962, JGR, 67, 1141
Tanaka, Y., Klemann, V., Martinec, Z., & Riva, R. E. M. 2011, GeoJI, 184, 220
Tanaka, Y., Klemann, V., & Martinec, Z. 2021, in IX Hotine-Marussi Symposium on Mathematical Geodesy, ed. P. Novák et al. (Cham: Springer), 157
Thyng, K. M., Greene, C. A., Hetland, R. D., Zimmerle, H. M., & DiMarco, S. F. 2016, Oceanography, 29, 9
Tyler, R. H., Henning, W. G., & Hamilton, C. W. 2015, ApJS, 218, 22
van der Wal, W., Barnhoorn, A., Stocchi, P., et al. 2013, GeoJI, 194, 61
Vance, S. D., Kedar, S., Panning, M. P., et al. 2018, AsBio, 18, 37
Čadek, O., Tobie, G., Van Hoolst, T., et al. 2016, GeoRL, 43, 5653
Wahr, J., & Bergen, Z. 1986, GeoJI, 87, 633
Wahr, J. M., Zuber, M. T., Smith, D. E., & Lunine, J. I. 2006, JGRE, 111, E12005
Watters, T. R., McGovern, P. J., & Irwin, R. P., III 2007, AREPS, 35, 621
Wieczorek, M. A., Neumann, G. A., Nimmo, F., et al. 2013, Sci, 339, 671
Williams, J. G., & Boggs, D. H. 2015, JGRE, 120, 689
Williams, J. G., Konopliv, A. S., Boggs, D. H., et al. 2014, JGRE, 119, 1546
Woodhouse, J. H., & Dziewonski, A. M. 1984, JGR, 89, 5953
Wu, P. 2004, GeoJI, 158, 401
Zambon, F., Mura, A., Lopes, R. M. C., et al. 2023, GeoRL, 50, e2022GL100597
Zerilli, F. J. 1970, JMP, 11, 2203
Zhong, S., Kang, K., & Qin, C. 2022, GGG, 23, e2022GC010359
Zhong, S., & Qin, C. A. G. 2012, GeoRL, 39, L15201
Zschau, J. 1978, in Tidal Friction in the Solid Earth: Loading Tides Versus Body Tides, ed. P. Brosche & J. Sündermann (Berlin: Springer), 62